ผลกระทบของแมงกานีสต่อสมบัติโฟโตลูมิเนสเซนซ์ของซิงค์ซัลไฟด์ที่สังเคราะห์ด้วยวิธีไมโครอิมัลชัน

นายณัฐธนัย รุ่งโรจน์มงคล

วิทยานิพนธ์นี้เป็นส่วนหนึ่งของการศึกษาตามหลักสูตรปริญญาวิศวกรรมศาสตรมหาบัณฑิต
สาขาวิชาวิศวกรรมเคมี ภาควิชาวิศวกรรมเคมี
คณะวิศวกรรมศาสตร์ จุฬาลงกรณ์มหาวิทยาลัย
ปีการศึกษา 2557

EFFECT OF MN ON PHOTOLUMINESCENCE OF ZNS SYNTHESIZED BY MICRO-EMULSION METHOD

Mr. Nattanai Rungrotmongkon

A Thesis Submitted in Partial Fulfillment of the Requirements

for the Degree of Master of Engineering Program in Chemical Engineering

Department of Chemical Engineering

Faculty of Engineering

Chulalongkorn University

Academic Year 2014

Thesis Title	EFFECT OF MN ON PHOTOLUMINESCENCE OF ZNS SYNTHESIZED BY MICRO-EMULSION METHOD
By	Mr. Nattanai Rungrotmongkon
Field of Study	Chemical Engineering
Thesis Advisor	Associate Professor Tawatchai Charinpanitkul, D.Eng.

Accepted by the Faculty of Engineering, Chulalongkorn University in Partial Fulfillment of the Requirements for the Master's Degree

.....Dean of the Faculty of Engineering
(Professor Bundhit Eua-arporn, Ph.D.)

THESIS COMMITTEE

.....Chairman
(Associate Professor Varong Pavarajarn, Ph.D.)

.....Thesis Advisor
(Associate Professor Tawatchai Charinpanitkul, D.Eng.)

.....Examiner
(Assistant Professor Apinan Soottitantawat, D.Eng.)

.....External Examiner
(Associate Professor Panu Danwanichakul, Ph.D.)

ณัฐธนัย รุ่งโรจน์มงคล : ผลกระทบของแมงกานีสต่อสมบัติโฟโตลูมิเนสเซนซ์ของซิงค์ซัลไฟด์ที่สังเคราะห์ด้วยวิธีไมโครอิมัลชัน (EFFECT OF MN ON PHOTOLUMINESCENCE OF ZNS SYNTHESIZED BY MICRO-EMULSION METHOD) อ.ที่ปรึกษาวิทยานิพนธ์หลัก: รศ. ดร.ธวัชชัย ชรินพาณิชกุล, 104 หน้า.

คุณสมบัติการเปล่งแสงของอนุภาคนาโนซิงค์ซัลไฟด์สามารถปรับปรุงได้ด้วยการโดปแมงกานีส ซึ่งอนุภาคนาโนซิงค์ซัลไฟด์โดปแมงกานีสสามารถเป็นตัวเลือกหนึ่งในการนำไปประยุกต์ใช้งานเกี่ยวกับอุปกรณ์ทางแสง เช่น เซลล์แสงอาทิตย์ อุปกรณ์รวบรวมแสงอาทิตย์ งานวิจัยนี้ได้มุ่งเน้นในการสังเคราะห์อนุภาคนาโนซิงค์ซัลไฟด์ที่ถูกแทรกด้วยแมงกานีสด้วยวิธีไมโครอิมัลชัน ซึ่งมีข้อดีคือสามารถควบคุมขนาดของอนุภาคในระดับนาโนเมตรได้ โดยอาศัยการควบคุมอัตราส่วนโมลของน้ำต่อโมลของสารลดแรงตึงผิว (W) ทั้งนี้ขนาดของอนุภาคนาโนซิงค์ซัลไฟด์ที่ถูกแทรกด้วยแมงกานีส และความเข้มข้นของแมงกานีสนั้นมีผลต่อสมบัติการเปล่งแสงของอนุภาคดังกล่าว ในงานวิจัยนี้ได้นำอนุภาคนาโนซิงค์ซัลไฟด์ที่ถูกแทรกด้วยแมงกานีสไปวิเคราะห์ด้วยเทคนิคต่างๆ เช่น การหักเหของรังสีเอ็กซ์ (XRD), การถ่ายภาพด้วยกล้องอิเล็กตรอนแบบส่องผ่าน (TEM) และกล้องอิเล็กตรอนแบบส่องกราด (FE-SEM) และการวัดค่าการเปล่งแสงด้วยเครื่องวัดการคายแสง (Spectrofluorometer) จากผลการวิเคราะห์พบว่าขนาดของอนุภาคนาโนซิงค์ซัลไฟด์ที่ถูกแทรกด้วยแมงกานีสมีขนาดที่ใหญ่ขึ้นเมื่อเพิ่มอัตราส่วนโมลของน้ำต่อโมลของสารลดแรงตึงผิว เนื่องจากผลกระทบของขนาดของรีเวอร์สไมเซลล์ นอกจากนี้ความเข้มของการเปล่งแสงจากแมงกานีสและซิงค์ซัลไฟด์ของอนุภาคซิงค์ซัลไฟด์ที่ถูกแทรกด้วยแมงกานีสเพิ่มขึ้น เมื่ออนุภาคปฐมภูมิมีขนาดเล็ก ส่วนการปรับค่าความเข้มข้นของแมงกานีสนั้น สัดส่วนความเข้มของการเปล่งแสงจากแมงกานีสต่อความเข้มแสงของการเปล่งแสงจากซิงค์ซัลไฟด์เพิ่มขึ้น เมื่อเพิ่มความเข้มข้นของแมงกานีส

ภาควิชา วิศวกรรมเคมี ลายมือชื่อนิสิต .....

สาขาวิชา วิศวกรรมเคมี ลายมือชื่อ อ.ที่ปรึกษาหลัก .....

ปีการศึกษา 2557

5470191421 : MAJOR CHEMICAL ENGINEERING

KEYWORDS: MN-DOPED ZNS NANOPARTICLES / MICRO-EMULSION / PHOTOLUMINESCENCE

NATTANAI RUNGROTMONGKON: EFFECT OF MN ON PHOTOLUMINESCENCE OF ZNS SYNTHESIZED BY MICRO-EMULSION METHOD. ADVISOR: ASSOC. PROF. TAWATCHAI CHARINPANITKUL, D.Eng., 104 pp.

Photoluminescence property of ZnS nanoparticles could be improved by doping other components, such as manganese. Mn-doped ZnS nanoparticles is one of promising candidates for application in novel devices, such as solar cell and solar concentrator. An aim of this research is set to synthesize Mn-doped ZnS nanoparticles via micro-emulsion method because of its advantage in controlling particle size of resultant nanoparticles via the molar ratio of water to surfactant (W). It is well recognized that nominal particle size and Mn concentration of Mn-doped ZnS nanoparticles affect photoluminescence property. The synthesized Mn-doped ZnS nanoparticles were characterized by X-ray diffractometer, transmission electron microscopy (TEM), field emission scanning electron microscopy (FE-SEM) and spectrofluorometer. For analyzed results, the primary particle size of Mn-doped ZnS nanoparticles increases when the molar ratio of water to surfactant increases because of effect of reversed micelle size. In addition, emission intensity from Mn and ZnS increases when primary particle size deceases. For various Mn concentrations, the relative emission intensity from Mn to emission intensity from ZnS increases when Mn concentration increases.

Department: Chemical Engineering Student's Signature .....

Field of Study: Chemical Engineering Advisor's Signature .....

Academic Year: 2014

ACKNOWLEDGEMENTS

I am very grateful to my thesis advisor, Assoc. Prof. Dr.Tawatchai Charinpanitkul, Department of Chemmical Engineering, Chulalongkorn University, for teaching and advice in this research, encouragement and kindness.

I would like to thank Associate Professor Dr. Varong Pavarajarn as chairman, Associate Professor Dr. Panu Danwanitkul as external examiner and Assistant Professor Dr. Apinan Soottitantawat as internal examiner for their interesting comments and participation as committee. I would like to thank all my teachers for their teaching and their advice.

I would like to thank and Faculty of Science, Mahidol University for their advice in TEM. I would like to thank The Central Instrument Facility (CFI), Mahidol University and National Nanotechnology Center (NANOTEC) for their advice in spectrofluorometer. I would like to thank The Scientific and Technological Research Equipment Centre for advice in XRD, TEM and FE-SEM. I would like to thank Synchrotron Light Research Institute (Public Oganization) for their advice XAS Beam Line 5.2. I would like to thank Department of Materials Science, Faculty of Science, Chulalongkorn University for their advice in XRD. I would like to thank Thailand Center of Excellence in Physic (ThEP), Chiang Mai University for their advice FE-SEM. I would like to thank National Metal and Materials Technology Center (MTEC) for advice zetasizer. I would like to thank Mr. Pongthon Roongcharoen, Department of Mining and Petroleum Engineering, Faculty of Engineering, Chulalongkorn University for suggestion of XRD and Photoluminescence results.

Thanks to Mrs. Pusanisa Patharachotesawate and my friends in the Center of Excellence in Particle Technology (CEPT), Department of Chemical Engineering, Faculty of Engineering, Chulalongkorn University and all of my friends for friendship, encouragement and their assistance especially all time.

Finally, I would like to extremely express my highest gratitude to my parents and family for their unconditional love and support everything in my life.

CONTENTS

Page

Page

Page

CHAPTER I

INTRODUCTION

1.1 Background

At present, nanotechnology has become one of the most important innovations in daily life. Many new product innovations can be improved by nanotechnology. Nanotechnology is based on the recognition that particle size less than 100 nanometers and nanostructure built from them new properties or behaviors. Many properties such as mechanics, electricity, magnetism and optics of semiconductors depend on the size [1]. Optical property is one of the interesting property for study and research because it is applied in electro-luminescence devices. The most investigated luminescent semiconductors are usually cadmium group materials such as cadmium selenide (CdSe), cadmium telluride (CdTe) and cadmium sulfide (CdS) [2-9] and zinc group materials such as zinc sulfide (ZnS) and zinc selenide (ZnSe). However, Cadmium group is not popular applications because of the intrinsic toxicity of Cd element [10]. In addition, ZnS is chemical stability and good photoluminescence more than ZnSe [11]. Therefore, ZnS is the most interesting semiconductor for research.

ZnS is one of the luminescent semiconducting nanocrystals. It has a direct band gap of 3.6 eV at room temperature [12]. Because ZnS is very good luminescent material, good chemical stable, low toxicity and low cost, it is applied in displays, sensors, lasers, catalysis, solar concentrator, photocatalyst, solar cell and

a biomolecular probe in fluorescence [13-19]. In addition, ZnS can easily host for doped metal impurity because it has a large band gap. There are two types of doping metal ions including rare earth metal ions and transition metal ions. Rare earth metal ions include europium (Eu^{3+}), [20-22], terbium (Tb^{3+}) [23,24] and erbium (Er^{3+}) [25]. In contrast, transition metal ions include copper (Cu^{2+}) [26,27], manganese (Mn^{2+}) [2,10,28-49]. However, dissimilarly chemical properties between rare earth metal ions and ZnS host, efficient doping of rare earth metal ions into ZnS host are not favorite [20]. On the other hand, the chemical properties of Mn are very similar to ZnS host, thus Mn ions incorporate into ZnS host much more easily [45]. Therefore, Mn is interesting for being doped into ZnS host. When Mn incorporate into Zn host, strong hybridization between the s-p states of ZnS host and d-state of Mn impurities lead to faster energy transfer between ZnS host and Mn impurities. Therefore, luminescent efficiency is increased and its lifetime is shorted from millisecond to nanosecond, in comparison with Mn-doped ZnS bulk [29]. Moreover, transfer of electron and hole of Mn-doped ZnS leads to characteristic emission from Mn $^4T_1$-$^6A_1$ transition [50].

There are many methods for synthesis of Mn-doped ZnS nanoparticles such as solvothermal [11,30], hydrothermal [33], precipitation [10,32,38,39,42,46] and micro-emulsion [31,36,48]. Among these methods, micro-emulsion is suitable for synthesis of Mn-doped ZnS nanoparticle because it possesses several advantages like ease of particle size control, narrow particle size distribution, soft chemical with simple handling and no need of special equipment.

Micro-emulsion method is a thermodynamically stable dispersion of two types of immiscible fluids. Water in oil (W/O) micro-emulsion could be formed when a water phase is enclosed by surfactant dispersed in an oil phase. The coexistence of oil phase, water phase and surfactant would generate the so-called reversed micelles.

Generally, cation and anion reagents could be encapsulated inside reversed micelles. If reversed micelles containing such cations and anions are taken into contact, a reaction between those ions would take place inside the reversed micelles, resulting in the precipitation of nanostructured product. In this sense, reversed micelles could be considered nanoreactor [51]. Later, it was found that adding co-surfactant into micro-emulsion system can enhance the interaction of reversed micelles. Therefore, effect of various co-surfactants added into micro-emulsion system for synthesizing ZnS was comprehensively examined and reported by Charinpanitkul et al. [52]. The previously in studies, effect of the molar ratio of water to surfactant and Mn concentration on photoluminescence property are not understood.

Hence, this research is aimed to study synthesis of Mn-doped ZnS nanoparticles by micro-emulsion method, to study influently synthesized method on the primary particle size, to study effect of the molar ratio of water to surfactant (W) on photoluminescence property of Mn-doped ZnS nanoaprticles and to study effect of Mn concentration on photoluminescence property of Mn-doped ZnS nanoaprticles.

1.2 Objective

To investigate effect of Mn on photoluminescence of ZnS synthesized by micro-emulsion method by taking into account the molar ratio of water to surfactant and concentration of Mn dopant.

1.3 Scopes of Research

Synthesis of Mn-doped ZnS nanoparticles was conducted as follows:

- Synthesized method: precipitation and micro-emulsion method for comparing the primary particle size of Mn-doped ZnS nanoparticles.
- The molar ratio of water to surfactant (W): 1, 3, 5, 7, 11 and 15 for control the primary particle size and study effect of the molar ratio of water to surfactant on photoluminescence property
- Mn concentration: 0, 6 and 10 percent by weight for study effect of Mn concentration on photoluminescence property
- Reactant concentration: 0.10, 0.25 and 0.50 M for study effect of reactant concentration on the primary particle size and amount of Mn-doped ZnS nanoparticles product

Characterizations of Mn-doped ZnS nanoparticles were used as follows:

- Morphology and the primary particle size of Mn-doped ZnS nanoparticles were examined by FE-SEM.
- Particles size distribution of Mn-doped ZnS nanoparticles was analyzed by Zetasizer.
- Crystalline structure of Mn-doped ZnS nanoparticles was determined by XRD, SAED and HRTEM.
- Photoluminescence property of Mn-doped ZnS nanoparticles was determined by spectrofluorometer.
- Local structure and oxidation number of Mn-doped ZnS nanoparticles were determined by EXAFS and XANES, respectively.

CHAPTER II

LITERATURE REVIEWS

2.1 Synthesis of ZnS nanoparticles via micro-emulsion method

Charinpanitkul et al. studied effect of co-surfactant and reactant concentration on zinc sulfide nanoparticles. They synthesized ZnS nanoparticles by micro-emulsion method and varied co-surfactant in n-butanol, n-pentanol and n-hexanol. When molecule of co-surfactant is larger, the aspect ratio of ZnS nanoparticle increases. In addition, ZnS nanorod and nanotube were formed when reactant concentration was increased [52].

Xu and Li studied formation of ZnS nanorod and nanoparticles in water in oil (W/O) micro-emulsion system. They used zinc sulfate and sodium sulfide as reactant and CTAB and Triton X-100 as surfactant. Morphology of ZnS is changed when varied the molar ratio of water to surfactant because of changing droplet sized of water pool in reversed micelle.The uniform ZnS nanorods could be prepared by using W = 11 at room temperature, 24 hours for aging time and using Triton X-100 as surfactant [53].

From the previous studies, ZnS nanoparticles can be synthesized by micro-emulsion method. The morphology of ZnS nanoparticles depends on type of surfactant and co-surfactant. Mn-doped ZnS nanoparticles will be possibly synthesized by micro-emulsion method the same as synthesized ZnS nanoparticles.

Then, the many previous researches about synthesized Mn-doped ZnS nanoparticles via micro-emulsion method were reviewed in the next section.

2.2 Synthesis of Mn-doped ZnS nanoparticles via micro-emulsion method

Gan et al. studied improvement of photoluminescence property. They compared micro-emulsion method and aqueous solution precipitation. Smaller the primary particle size and narrower particle size distribution were observed when synthesis of Mn-doped ZnS nanoparticles via micro-emulsion method. Moreover, they compared photoluminescence property between both synthesis methods. Mn-doped ZnS nanoparticles were surface passivated at temperature of 120 °C. Photoluminescence intensity is higher when Mn-doped ZnS nanoparticles are synthesized by micro-emulsion method and surface passivation [31].

Murugadoss studied structure, optical and thermal characterization of Mn-doped ZnS nanoparticles synthesized by reversed micelle method. Particles size of Mn-doped ZnS nanoparticles from TEM photographs was smaller when adding co-surfactant into micro-emulsion system. Reactant concentration and Mn concentration were fixed with 0.50 molar and 4% by weight, respectively. From TEM analysis, the averaged particles size increases when the molar ratio of water to surfactant (W) increases from 8 to 11. The XRD patterns confirmed zinc blend crystal structure of Mn-doped ZnS nanoparticles. Moreover, photoluminescence intensity is the highest as the molar ratio of water to surfactant about 10. In addition, Mn-doped ZnS nanoparticles products were heated at 200-800 °C for 2 hr. At temperature of 200 °C, Mn-doped ZnS nanoparticles became ZnO because it was oxidized by oxygen gas in the air [36].

In these the previous works, Mn-doped ZnS nanoparticles were synthesized by micro-emulsion method. Photoluminescence property of Mn-doped ZnS nanoparticles is higher when synthesized Mn-doped ZnS nanoparticles by micro-emulsion method. Although the effect of the molar ratio of water to surfactant on the primary particle size has been investigated, the effect of the primary particle size on photoluminescence property is lacking. This is a point for studied the effect of the primary particle size on photoluminescence property. In addition, Mn concentration could be possible to affect photoluminescence. Therefore, the many previous researches about effect of Mn concentration on photoluminescence property were reviewed in the next section.

2.3 Synthesis of Mn-doped ZnS nanoparticles at various Mn concentrations

Peng et al. observed photoluminescence and magnetic property of synthesized Mn-doped ZnS nanoparticles by co-precipitation. They varied Mn concentration within 5-15 % by atom. The XRD patterns confirmed zinc blend crystalline structure of Mn-doped ZnS. As Mn concentration increases, photoluminescence intensity and magnetic property increases. All synthesized Mn-doped ZnS nanoparticles showed paramagnetic property [10].

Dong et al. synthesized Mn-doped ZnS nanoparticles with finely controlled reaction temperature and doping levels via solvothermal method. 1% by mole of Mn-doped ZnS nanoparticles as different reaction temperature were analyzed by TEM. The averaged particle size increases when reaction temperature decreases. SAED patterns of samples are consistent with zinc blend ZnS crystalline structure with ring pattern. XRD patterns confirmed zinc blend crystalline structure of Mn-doped ZnS.

While the reaction temperature increases, the ZnS emission intensity decreases but the Mn emission intensity increases [11].

Hoa et al. investigated photoluminescence property of Mn-doped ZnS nanoparticles. They synthesized Mn-doped ZnS nanoparticles via hydrothermal. From XRD patterns, synthesized Mn-doped ZnS were zinc blend crystalline structure. Mn concentration of synthesized Mn-doped ZnS nanoparticles are in range 0-20 % by atom. When Mn concentration is 0% by atom, blue emission peak of ZnS was observed at 490 nm. Orange emission peak of Mn was observed at 588 nm, when Mn concentration was more than 0% by atom. In addition, orange emission intensity maximized at 1% by atom [33].

Sarkar et al. synthesized Mn-doped ZnS nanoparticles by chemical precipitation method. Mn concentration was varied in range 0-2.5%. XRD patterns confirmed zinc blend crystal structure of all samples. The averaged crystalline size was approximately 3 nm calculated by Debye-Scherrer formula. From TEM images, the averaged primary particle sizes were 2.2 nm for un-doped ZnS and 2.9 nm for 1% Mn-doped ZnS nanoparticles. Photoluminescence intensity of Mn-doped ZnS nanoparticles increases when Mn concentration increases [39].

Tripathi et al. studied photoluminescence property of Mn-doped ZnS nanoparticles. XRD patterns confirmed zinc blend crystalline structure of Mn-doped ZnS. Mn concentration was varied in a range 0-5% by atom. Photoluminescence intensity maximized as 5% by atom of Mn concentration [42].

Han et al. synthesized Mn-doped ZnS nanoparticles by precipitation method. They studied effect of Mn doping concentration and surfactant concentration on photoluminescence property. XRD patterns of Mn-doped ZnS nanoparticles prepared with methacrylic acid (MAA), cetyltrimethylammonium (CTAB) and without surfactant confirmed zinc blend crystal structure. From SEM images, the averaged primary particle size of Mn-doped ZnS nanoparticles prepared with MMA, CTAB and without surfactant were around 10-20 nm. Photoluminescence intensity of Mn-doped ZnS nanoparticles synthesized with varying amount of MAA is highest when concentration of MAA is 0.345 moles. Photoluminescence intensity of Mn-doped ZnS nanoparticles synthesized with varying amount of CTAB is highest when concentration of CTAB is 0.125 moles. Therefore, comparing photoluminescence intensity of Mn-doped ZnS nanoparticles prepared with MAA, CTAB and without surfactant, photoluminescence intensity of Mn-doped ZnS nanoparticles prepared with MAA is the highest. In addition, photoluminescence intensity of Mn-doped ZnS is the highest as 0.08 mole of Mn concentration [32].

Cao et al. observed Mn dopant for orange emission spectrum of Mn-doped ZnS nanoparticles. Mn-doped ZnS nanoparticles were synthesized by solvothermal. Mn concentration was varied in range 0-11% by atom. XRD patterns confirmed mainly zinc blend structure and small amount of ZnS in wurzite structure of Mn-doped ZnS. TEM and HRTEM images of Mn-doped ZnS nanoparticles are observed that these nanoparticles are agglomerated with diameter 12-18 nm. From XANES spectrum, Mn ions were substitutionally incorporated into the ZnS lattice and no Mn related secondary phase was formed. Photoluminescence intensity is maximized at level of 3% by atom of Mn-doped ZnS nanoparticles [30].

Xiao et al. synthesized Mn-doped ZnS nanoparticles by using thioglycolic acid (TGA) as a stabilizer in aqueous solution in air. They varied Mn concentration in a range 0-3% by weight. XRD patterns confirmed zinc blend crystalline structure of Mn-doped ZnS. The averaged crystalline sizes for different Mn concentration (0, 1.5 and 3% by weight) were estimated to be 1.96, 2.04 and 2.11 nm, respectively. Photoluminescence spectra of un-doped samples showed only one emission band at 460 nm. On the other hand, photoluminescence spectrums of Mn-doped ZnS nanoparticles show two different emission bands at 460 nm emitted from ZnS host and 585 nm emitted from Mn impurities. Emission intensity of Mn-doped ZnS nanoparticle increases when Mn concentration increases and shows a maximum intensity as 1.5 wt. % [44].

Nazerdeylami et al. synthesized Mn-doped ZnS nanoparticles by chemical method using PVP (Polyvinylpyrrolidone) as a capping agent in aqueous solution. They varied Mn concentration about 1, 5 and 10% by mole. XRD patterns confirmed zinc blend crystalline structure of all Mn-doped ZnS samples and no diffraction peak from Mn impurities. The averaged crystalline sizes of Mn-doped ZnS with different concentration (1%, 5% and 10% were estimated to be 2.35, 2.24 and 2.30 nm, respectively. Photoluminescence spectra centered observed at 594 nm emitted from Mn impurities. Mn concentration increases resulting in emission intensity increases. In addition, maximum Mn emission intensity and minimum Zn emission intensity were found at Mn concentration of 10 wt. % [37].

From the many previous studies, the optimum Mn concentration likely depended on the synthesis methods of Mn-doped ZnS nanoparticles. Therefore, it is a point for studying effect of Mn concentration on photoluminescence property of Mn-doped ZnS nanoparticles synthesized by micro-emulsion method.

CHAPTER III

THEORIES AND EXPERIMENTAL

3.1 Theories

3.1.1 Physical and Chemical Properties of Zinc sulfide

Zinc sulfide is an inorganic compound with the formula ZnS. ZnS is a white powder. This is the main form of zinc found in nature, where it mainly occurs as the mineral sphalerite. There are two crystal structures of ZnS with zinc blend and wurtzite as schematically shown in Figure 3.1. The transition from sphalerite become wurtzite at temperature of 1,020 °C

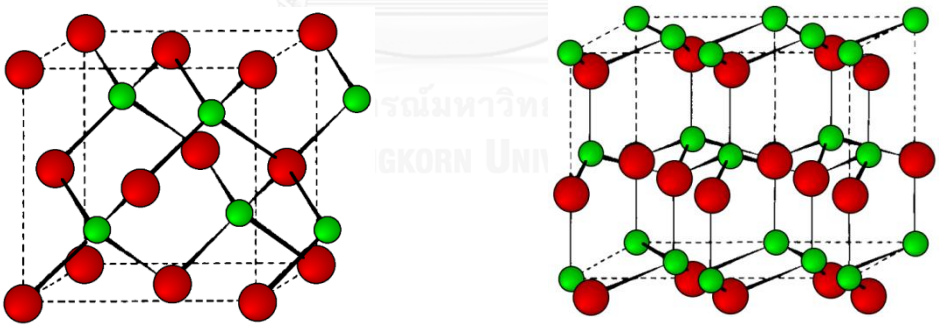

(a) (b)

Figure 3.1 ZnS crystalline structures: (a) zinc blend structure, (b) wurzite structure, reprinted in reference [54]

3.1.2 Solid Solutions

A solid solution is formed when the solute atoms are added to the host material, the crystalline structure is maintained and no new structures are formed. A solid solution is compositionally homogeneous. The impurity atoms are randomly and uniformly dispersed in host material. Impurity point defects are found in solid solutions. Two types of defects are substitutional and interstitial type. For the substitutional type, impurity atoms replace or substitute for the host atoms as shown in Figure 3.2.

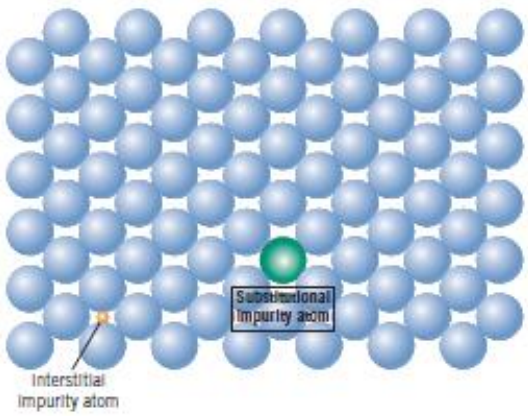

Figure 3.2 Schematic substitutional and interstitial impurity atoms, reprinted in reference [55]

Several features of the solute and solvent atoms were determined by the degree of the former dissolves in the latter, as follows:

1. Atomic size factor

Solute materials may be accommodated in this type of solid solution only when the difference in atomic radii between these two atoms are ±15%. Otherwise the solute atoms will create substantial lattice distortions and a new phase will form.

2. Crystalline structure

The crystalline structures for both metals atoms must be the same.

3. Electronegativity

More electropositive and electronegative is greater than the likelihood that they will form an intermetallic compound instead of a substitution in solid solution.

For interstitial solid solutions, impurity atoms fill the voids among the host atoms as represented in Figure 3.2. The atomic diameter of an interstitial impurity must be substantially smaller than the atomic diameter of the host atoms. Normally, the maximum allowable concentration of interstitial impurity atoms is low (less than 10%). Even very small impurity atoms are ordinarily larger than the interstitial sites, and as a consequence they introduce some lattice strains on the adjacent host atoms [55].

3.1.3 Specification of composition

The composition or concentration of an alloy in terms of its constituent elements. Type of specific composition consist of percent by weight (or mass) and percent by mole [55]. The basis for weight percent (wt. %) is the weight of a particular element relative to the total alloy weight. For an alloy that contains two hypothetical atoms denoted by 1 and 2, the concentration of 1 in wt. %, C_1, is defined as equation 3.1 where m_1 and m_2 represent the

$$C_1 = \frac{m_1}{m_1+m_2} \times 100 \quad (3.1)$$

weight or mass of elements 1 and 2, respectively. The basis for mole percent (mole %) calculations is the number of moles of an element in relation to the total

moles of the elements in the alloy. The number of moles in some specified mass of element 1, n_{m1}, may be computed as follows:

$$n_{m1} = \frac{m_1}{A_1} \tag{3.2}$$

Here, m_1 and A denote the mass (in grams) and atomic weight, respectively, for element 1. Concentration in terms of mole percent of element 1 in an alloy containing element 1 and element 2, is defined by equation 3.3.

$$C_1' = \frac{n_{m1}}{(n_{m1}+n_{m2})} \times 100 \tag{3.3}$$

3.1.4 Energy Band and Structures in Semiconductor

The possible electronic band of semiconductor at temperature of 0 Kelvin was shown in Figure 3.3. In Figure 3.3, the valence band is completely filled with electrons, while the empty conduction band has no electron occupied. An energy gap between valence band and conduction band is an energy band gap (E_g). For very pure materials, electrons have no energies within this gap. The band gap of insulator is wide while the band gap of semiconductors is narrow. The Fermi energy for these two band structures lies within the band gap near its center [55].

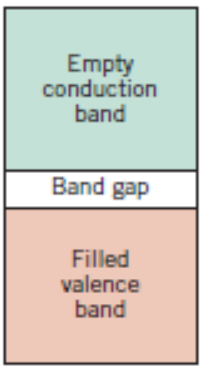

Figure 3.3 Energy band of semiconductor at temperature of 0 Kelvin, reprinted in reference [55]

3.1.5 Conduction in Term of Band and Atomic Bonding Models

When the only electrons energy is greater than the Fermi energy (E_f), the electrons may be acted on and accelerated in the presence of an electric field. These are the electrons that participate in the conduction process which are termed free electrons. Another charged electronic entity called a hole is found in semiconductors. Holes have energies less than E_f and also participate in electronic conduction.

For semiconductors, electrons in the highest occupied molecular orbital (HOMO) can be promoted across the energy band gap to fill in the lowest unoccupied molecular orbital (LUMO). The energy between HOMO and LUMO is approximately equal to the band gap energy (E_g). This excitation process is illustrated in Figure 3.4. For many materials, this band gap is several electron volts wide. Most often the excitation energy is from a nonelectrical source such as heat or light. The number of electrons excited by heat energy into the conduction band depends on the energy band gap width at constant temperature [55].

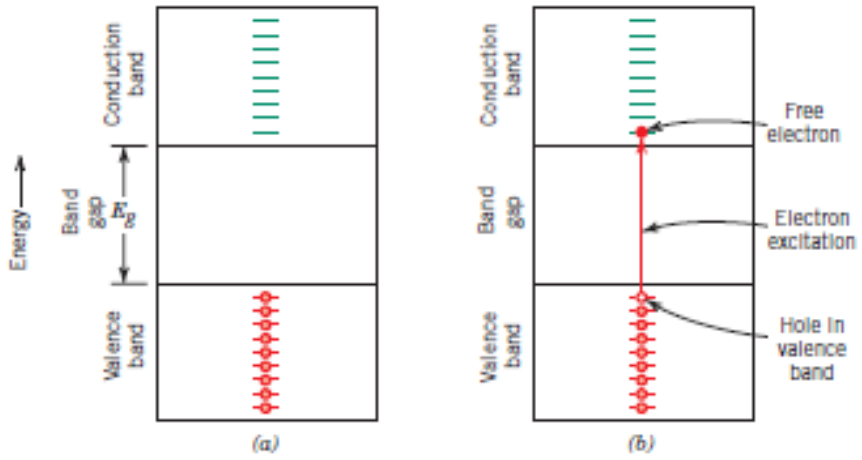

Figure 3.4 Occupancy of electron states of semiconductor (a) before and (b) after an electron excitation from the valence band into the conduction band, reprinted in reference [55]

3.1.6 Quantum Well, Quantum Wire and Quantum Dot

From elementary quantum mechanics, when electronic particles (electrons and holes) are confined by potential barriers to regions of space that are smaller than the de Broglie wavelength of the particles. The allowed energy states become discrete (i.e., quantized). For semiconductors, the critical dimension for quantization effects depends on the effective mass of the electronic charge carriers. Since quantization depends on spatial confinement, three regimes the quantum well, quantum wire and quantum dot (nanocrystal) have the confinement in one, two and three dimensions, respectively (Figure 3.5). The quantum dot is the most common product of small semiconducting particles.

Some fundamental differences exist for the three regimes of size quantization. First, the density of electronic states (DOS) is a function of energy for three regimes as illustrated in Figure 3.6. For quantum well, the DOS is a step function. For quantum dot, it is a series of discrete values, like a molecule or atom. Quantum wire has a DOS distribution that is intermediate between quantum well and quantum dot [56].

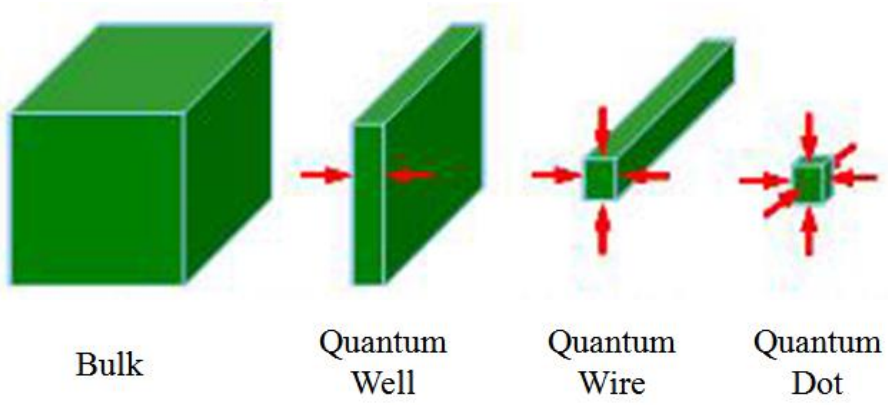

Figure 3.5 Quantization configuration type in semiconductors, reprinted in reference [57]

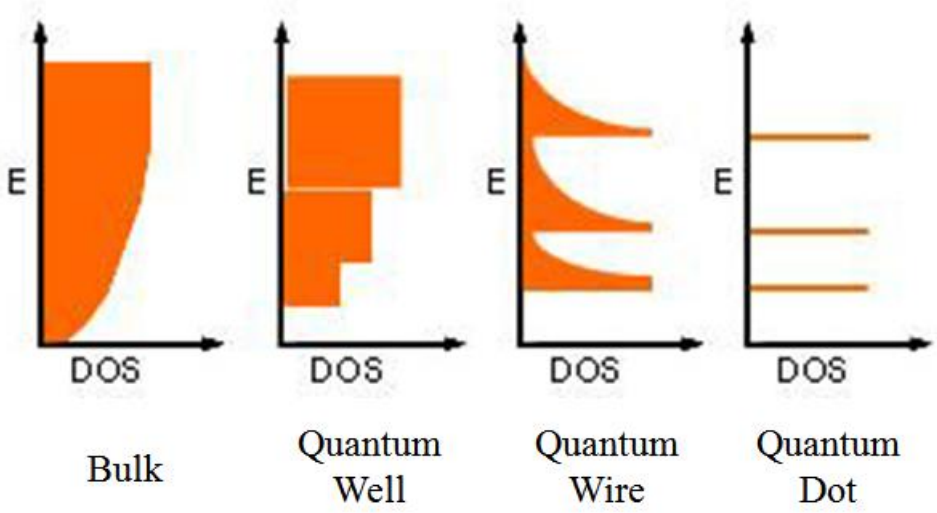

Figure 3.6 Density of electronic state (DOS) function for bulks, quantum wells, quantum wires and quantum dots, reprinted in reference [57]

3.1.7 Luminescence

Luminescence is a phenomenon of excited molecule and then emitted in from of visible light [55,58]. If source of energy is the light, it will be called "photoluminescence". In addition, photoluminescence is classified according to the magnitude of the delay time between absorption and reemission events. For reemission time less than one second, the phenomenon is called "fluorescence". When reemission occurs longer times, it is called "phosphorescence". A number of materials including some sulfides, oxides and organic materials are fluorescence or phosphorescence.

Interactions with light radiation can also occur in dielectric solids having wide band gaps. If impurities or other electrically active defects are present, electron levels within the band gap may be introduced such as the donor and acceptor levels. Light radiation of specific wavelengths may be emitted as a result of electron transitions within the band gap. The valence band–conduction band electron

excitation for impurity doped in material level as shown in Figure 3.7a. The electromagnetic energy was absorbed by electron excitation. Figure 3.7b shows the emission of two photons. One is emitted as the electron drops from a state in the conduction band to the impurity level while other photons emitted from impurity level into the valence band. In addition, one of the transitions may involve the generation of a phonon or heat energy as shown in Figure 3.7c.

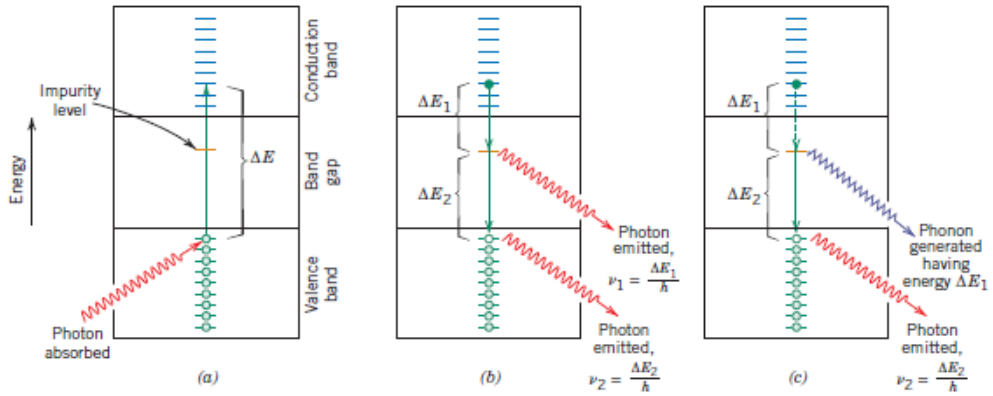

Figure 3.7 Absorption and emission of impurity doped semiconductor. (a) Photon absorption for a material that has an impurity level, (b) emission of two photons, (c) generation of a phonon and a photon, reprinted in reference [55]

3.1.8 Micro-Emulsion

Micro-emulsion is thermodynamically stable dispersion of oil and water, which could be stabilized by adding surfactant. Thermodynamic stability of micro-emulsion is temperature and pressure dependence. Schulman and his group first scientifically described micro-emulsion in 1943 [59]. The term “micro-emulsion” was first coined in 1959 by Schulman and his group [60]. Micro-emulsion is like transparent emulsion, swollen micelle and micellar solution. Winsor has classified different types of micro-emulsion system [61]. When oil in water (O/W) micro-emulsion is in equilibrium with excess oil, it is called “Winsor I”. The water in oil (W/O)

micro-emulsion is in equilibrium with excess water, it is called “Winsor II”. Micro-emulsion equilibrium with both oil and water is called “Winsor III”. This is a bicontinuous micro-emulsion in which both W/O and O/W dispersions. “Winsor IV” is not equilibrium either in oil or water.

The basic difference between micro-emulsion and emulsion is droplet size. The droplet size of micro-emulsion is smaller than 100 nm. In some systems, droplet sizes lie in between emulsion and micro-emulsion, this systems are called mini-emulsion. Both emulsions and mini-emulsions are not thermodynamically stable, but they are kinetically stable. The stability of emulsion and mini-emulsion is a function of time. In addition, emulsion is not microstructure and nontransparent.

The formation of micro-emulsion is explained by Gibbs free energy of mixing between oil and water. At a constant temperature and pressure, the water/oil interfacial tension (IFT, γ) = $\left(\frac{\partial G}{\partial A}\right)_{T,P}$. When IFT is positive, Gibbs free energy change is also positive. Hence, this system is not mixing. The water/oil interfacial tension (IFT, γ) must be zero or negative value. Therefore, addition of surfactant and co-surfactant leads to a very low IFT value. The energy of mixing between oil and water is defined in equation 3.4 where ΔG, ΔH, ΔS, T and ΔA are Gibbs free energy change, enthalpy change, entropy change, temperature (K) and change in interfacial area, respectively.

$$\Delta G = \Delta H - T\Delta S + \gamma\Delta A \quad (3.4)$$

The enthalpy change is negligible when immiscible oil and water are mixed. As the droplet size decease, entropy change is positive ($T\Delta S >> \gamma\Delta A$). Therefore, ΔG is negative for this system leading to dispersion of O/W and W/O becomes spontaneous and stable [62].

Generally, surfactant consists of polar and non-polar molecules. When surfactant was added in mixture of water and oil, the surfactant molecules associate spontaneously to form reversed micelle or micelle as shown in Figure 3.8. Surfactant concentration exceeds a certain minimum with a formation of micelle or reversed micelle, called “critical micelle concentration (CMC)” [63]. The shape of micelle or reversed micelle can be controlled by packing parameter of surfactant molecule. This packing parameter of surfactant molecule is defined with $\frac{V}{A \cdot L}$. Where V is the surfactant hydrocarbon volume, A is the polar head area and L is the fully extended chain length of the surfactant. At $\frac{V}{A \cdot L} > 1$, reversed micelle is formed. In contrast, micelle can be formed when this ratio is < 1 [64]. Spherical micelles are formed when the packing parameter is less than 1/3. Cylinder micelles and lamellar micelles are formed when the packing parameter are 1/2 and 1, respectively. Reversed micelles structures are formed when the packing parameter is greater than 2. Cylinder reversed micelles are formed at $\frac{V}{A \cdot L} \geq 2$, while spherical reversed micelles are presented at $\frac{V}{A \cdot L} > 3$. Schematic reversed micelle and micelle are shown in Figure 3.8. In addition, lamellar phase or bicontinuous micro-emulsion has $\frac{V}{A \cdot L} \approx 1$ [65]. Moreover, the molar ratio of water to surfactant (W) < 15 suggests a formation of reversed micelles [66].

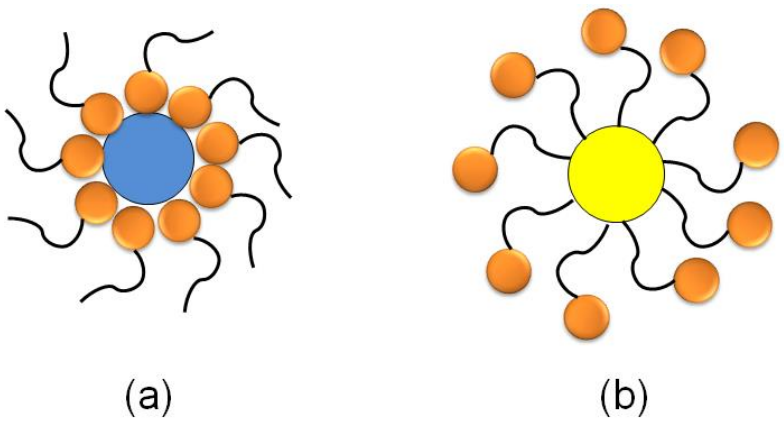

Figure 3.8 Type of micelle: (a) reversed micelle and (b) micelle

Reaction mechanism in micro-emulsion can be explained by nucleation in micro-emulsion system. Cations and anions reagents dissolve inside central core or water pool of reversed micelles. If we mix both reagents, reversed micelles are frequently collide via random Brownian motion and coalesce to form dimer which exchange cation and anion and then break apart again [67,68]. This results to the precipitation inside reversed micelles. Reversed micelle in this system can be called “nanoreactors”, resulting in controlled nucleation and particle growth [51]. Reaction mechanism in micro-emulsion was illustrated in Figure 3.9.

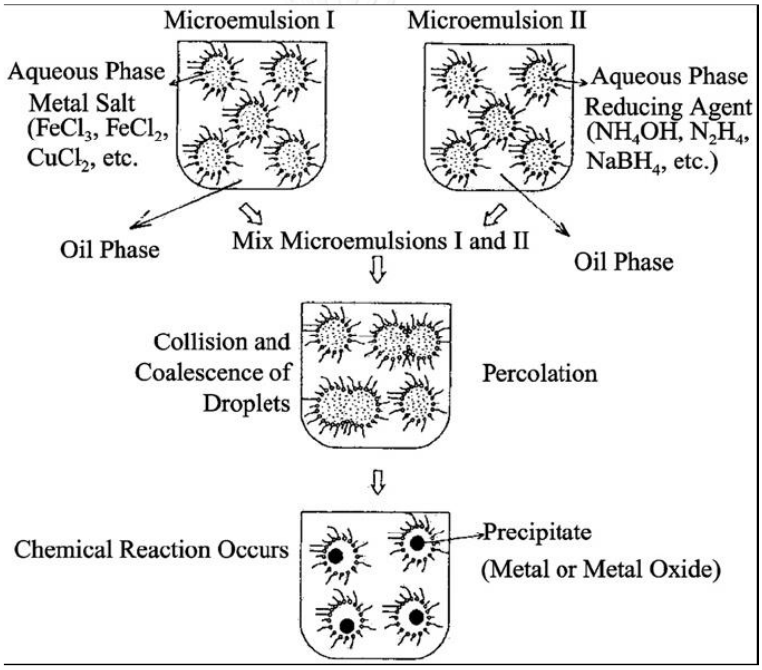

Figure 3.9 Reaction mechanisms in micro-emulsion system, reprinted in reference [63]

In addition, water in oil micro-emulsion is favorable for synthesis of nanoparticles because of the advantages of micro-emulsion method as fallows;

1. Ease of particles size control
2. Uniform and narrow particles size distribution
3. Soft chemical with simply handling
4. No need of special equipment

3.1.9 Crystallization

The crystallization from solution can occur when solute concentration in solvent exceeds solubility of solute. This solution will be called supersaturated solution. Supersaturated solution can be generated when two or more solute reactants react and produce very low solubility of product. This reaction processes are often precipitation processes.

Nucleation process is generation of nuclei. Such nuclei are formation of ions clusters. Nucleation and crystal growth were described by Gibbs. The energy change resulting from crystal nucleating homogeneously from solution is given by

$$\Delta G = \Delta G_S + \Delta G_V \quad (3.5)$$

where G_S is the free energy change required to from the surface of the nucleus and G_V is the free energy change resulting when solute changes from liquid to solid state and is a function of supersaturation level. G_S and G_V are proportional to the surface area and the nucleus volume, respectively. Assuming a spherical nucleus, equation 3.5 can be written as

$$\Delta G = 4\pi r^2 \delta + \frac{4}{3}\pi r^3 \Delta G_V \quad (3.6).$$

The nucleus radius is r, δ is the specific surface energy and ΔG_V is the bulk free energy change per unit volume. If the growth cluster larger than r_c will result in a decrease in free energy. It is presumed that in supersaturated solution, clusters are constantly forming and dispersing. Only cluster size larger than r_c becomes nuclei. Effect of solubility of small crystal on solution concentration can be represent in Gibb-Thomspson equation as shown in equation 3.7.

$$\ln\left(\frac{C_S}{C^*}\right) = \frac{2\delta\nu}{k_B T r_C} \tag{3.7}$$

Where C_S, C^*, ν, k_B and T are solution concentration, saturated concentration, the molecular volume, Boltzmann's constant and temperature in Kelvin, respectively. For the homogeneously nucleation rate (B^0) can be similarly expressed by Arrhenius type equation,

$$B^0 = C \exp\left(-\frac{16\pi\delta^3\nu^2}{3k^3T^3\left(\ln\frac{C_S}{C^*}\right)}\right) \tag{3.8}.$$

Equation 3.8 can be approximated by power law function of supersaturation. A proposed equation of power law, observing fact that nucleation does not occur at very low supersaturation. It is based on the concept of the metastable limit. In most inorganic system concentration at the metastable limit close to concentration at supersaturation, the equation can be written

$$B^0 = k(c - c_S)^i \tag{3.9}$$

where c, c_s and i are solution concentration, concentration at supersaturation and empirical exponent, respectively. In addition, Meirs model is more nearly analogous to those used in the reaction kinetic and the rate constant (k_R) is a function of temperature. Thus, the Meirs model can be written as

$$B^0 = k_0 \exp\left(-\frac{\Delta E_a}{kT}\right)(c - c_S)^i \quad (3.10)$$

where ΔE_a is the activation energy of the reaction.

A crystal growth mechanism from solution requires that solute transported to the crystal surface and then make of the crystal lattice. It can be explained by mass diffusion on the crystal surface. In general, the growth models are independent of species involved in growth process, these species affect the magnitude of the diffusion coefficient or of the surface reaction rate constant. If growth rate is limited by the rate of diffusion through growing laminar layer of solution, it can be called “diffusion controlled”. The diffusion controls are used in many cases of non-agitated systems. The growth rate is represented by simple mass transfer equation in equation 3.11.

$$\frac{dM}{dt} = \frac{D}{x} A_C (c - c_S) \quad (3.11)$$

Where D, x, A and $c-c_s$ are diffusion coefficient, film thickness, the surface area of the crystal the difference between the actual concentration and the saturated concentration, respectively. The crystal growth in this system was controlled by diffusion of ions to surface area of nuclei. The crystal rate increases when the velocity of supersaturated solution increases relatively to the crystal surface [69].

3.2 Chemical agents

The lists of the chemicals employed for synthesis of Mn-doped ZnS nanoparticles and the list of chemical agents produced by each company as representing in Table 3.1 and Table 3.2 respectively.

Table 3.1 List of chemical agents are using synthesis Mn-doped ZnS nanoparticles.

Chemical agents	Using for
1. Zinc Sulfate ($ZnSO_4 \cdot 7H_2O$)	Synthesis of Mn-doped ZnS
2. Sodium Sulfide ($Na_2S \cdot 9H_2O$)	Synthesis of Mn-doped ZnS
3. Manganese (II) Sulfate ($MnSO_4 \cdot H_2O$)	Synthesis of Mn-doped ZnS
4. Deionization water (H_2O)	Water Phase
5. Cyclohexane (C_6H_{12})	Oil Phase
6.Triton X-100 $C_{14}H_{22}O(C_2H_4O)$ (n = 9-10)	Surfactant
7. 1-Octanol ($C_8H_{15}O$)	Co-surfactant

Table 3.2 The lists of chemical agents are produced by each company.

Chemical agents	Company
1. Zinc Sulfate ($ZnSO_4 \cdot 7H_2O$) AR Grade	Ajax Finechem Pty Ltd.
2. Sodium Sulfide ($Na_2S \cdot 9H_2O$) AR Grade	Carlo Erba Reagents
3. Manganese (II) Sulfate ($MnSO_4 \cdot H_2O$) AR Grade	Carlo Erba Reagents
4. De-ionized water (H_2O)	-
5. Cyclohexzane (C_6H_{12}) AR Grade	QRec
6. Triton X-100 $C_{14}H_{22}O(C_2H_4O)_n$ (n = 9-10) AR Grade	Panreac Quimica S. L. U.
7. 1-Octanol ($C_8H_{15}O$) AR Grade	Panreac Quimica S. L. U.

3.3 Synthesis of Mn-doped ZnS nanoparticles

In this research, all samples of Mn-doped ZnS nanoparticle were synthesized under 30 ℃ of temperature and 1 atm of pressure.

3.3.1 Synthesis of Mn-doped ZnS nanoparticles by micro-emulsion method as various the molar ratios of water to surfactant (W) in a range 1, 3, 5, 7, 11 and 15

Mn-doped ZnS nanoparticles were prepared in cyclohexane/ Triton X-100/1-octanol water in oil reversed micelles via the micro-emulsion method. Firstly, the micro-emulsion was prepared by mixing 50 ml of cyclohexane, 14 ml of Triton X-100 and 3.7 ml of 1-octanol in continuously stirred beaker. Then an aqueous solution of $ZnSO_4$ and $MnSO_4$ was added into a micro-emulsion while an aqueous solution of Na_2S was added into another. The volume of aqueous solution was controlled by each the molar ratio of water to surfactant condition while the volume of surfactant and co-surfactant was fixed. Total volume of water phase was added in micro-emulsion system for each W. Concentration of $ZnSO_4$, $MnSO_4$ and Na_2S was fixed with 0.099, 0.100 and 0.001 M, respectively. After stirring, both micro-emulsions were mixed under continuous stirring condition to ensure complete mixture. And then, mixed both micro-emulsions slowly drop by drop and with continuous stirring for 2 hours. After being left quiescently under the ambient temperature for 10 hours, white powder was observed. Finally, the precipitated sample was washed by ethanol and de-ionized water in several times, filtrated and dried in hot air oven at temperature of 100 ℃ for 1 hour. The products are in the further characterization. This experimental procedure is represented in Figure 3.10.

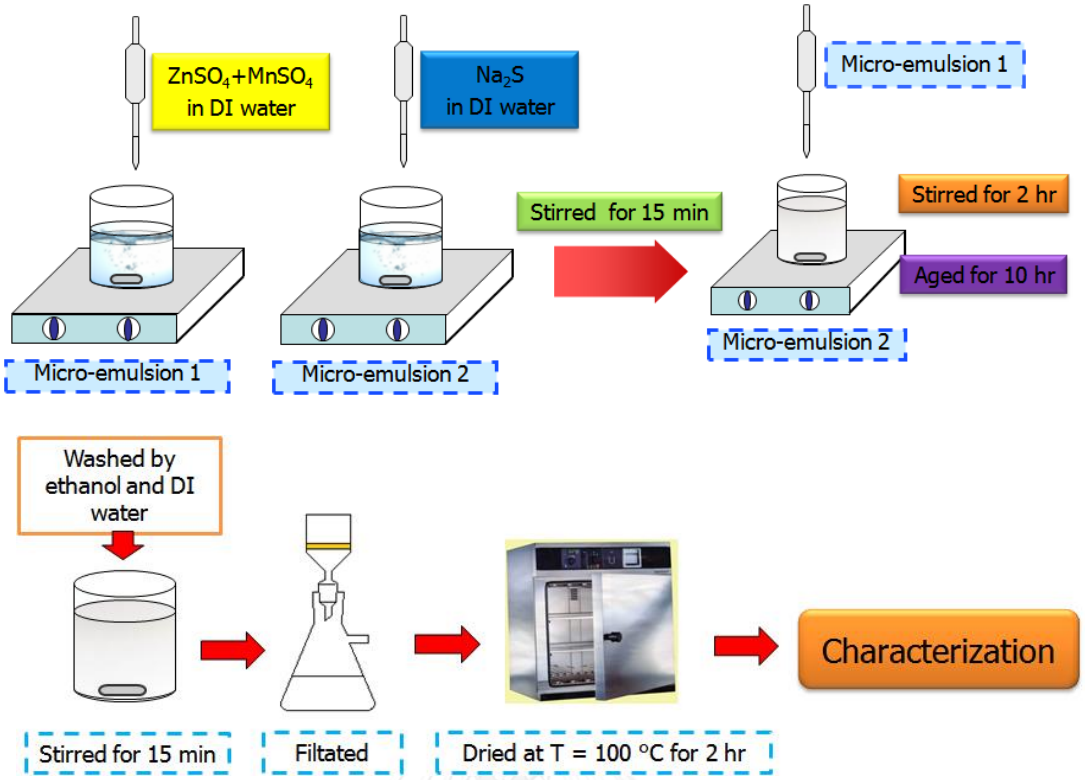

Figure 3.10 Experimental procedure of synthesized Mn-doped ZnS nanoparticles by micro-emulsion method

3.3.2 Synthesis of Mn-doped ZnS nanoparticles by precipitation method

The molar ratio of water to surfactant and concentration are constant. Concentration of $ZnSO_4$, $MnSO_4$ and Na_2S are 0.099, 0.001 and 0.100 M, respectively. Then, Na_2S solution was dropped into beaker $ZnSO_4$ and $MnSO_4$ solution and continuously stirring for 2 hours. After stirring time, the mixture was aged for 10 hours at room temperature (30 °C). Then, the mixture was washed by ethanol and de-ionized water in several time, filtrated and dried in hot air oven at 100 °C for 1 hours. The products will be characterized further. This experimental procedure is represented in Figure 3.11.

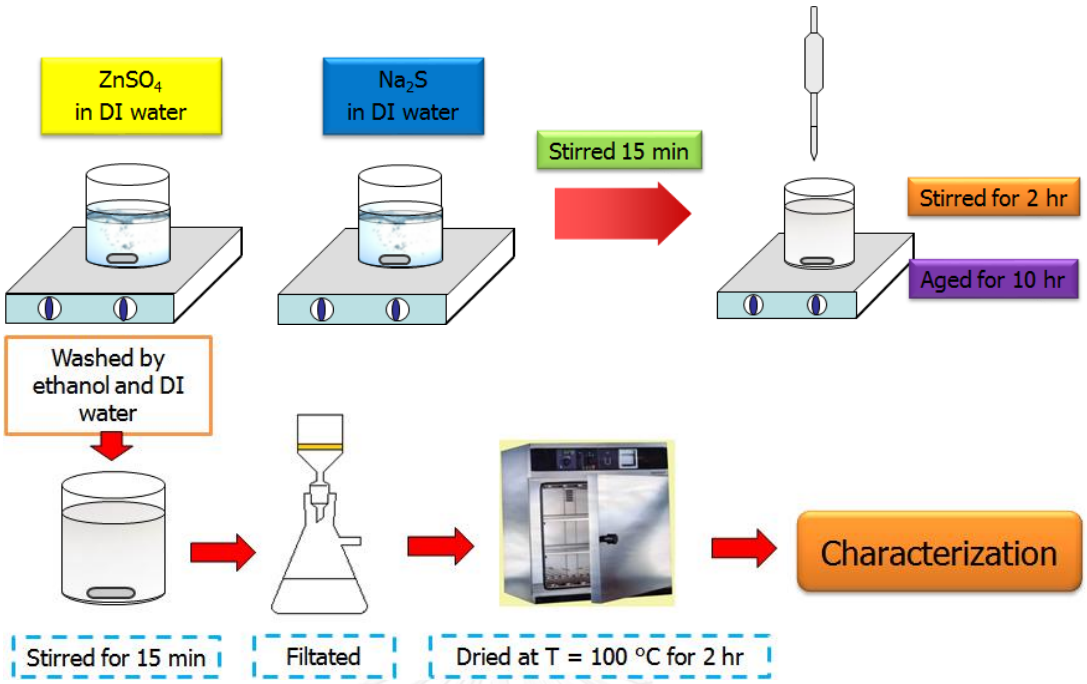

Figure 3.11 Experimental procedure of synthesized Mn-doped ZnS nanoparticles by precipitation method

3.3.3 Synthesis of Mn-doped ZnS nanoparticles by micro-emulsion method at various Mn concentrations with 0, 6 and 10 % by weight

This experimental procedure is the same section of 3.3.1 but changed weight ratio of Mn to Zn following condition of scope in Table 3.3 while the molar ratio of water to surfactant is constant as 1.

Table 3.3 Mn concentration at various weight ratios of Mn to Zn

Mn (wt. %)	Weight ratio of Mn to Zn
0	0/100
6	6/94
10	10/90

3.3.4 Synthesis of Mn-doped ZnS nanoparticles by micro-emulsion method at various reactant concentrations.

Reactant concentration in this experimental were used as followed in Table 3.4. The experimental procedure is the same section of 3.3.1 but changing reactant concentration while the molar ratio of water to surfactant and weight ratio of Mn to Zn were constant as 1 and 6/94, respectively.

3.4 Characterization of Mn-doped ZnS nanoparticles

The morphology and particle size were analyzed by FE-SEM Particle size distribution of samples was determined by particle size analyzer or zetasizer. Crystalline structure of samples was analyzed by TEM and XRD (Bruker D8 Discover). Photoluminescence property was analyzed by spectrofluorometer. Then, local structure and oxidation number were determined by XAS.

3.4.1 X-ray diffractometer (XRD)

X-ray diffractometer is important for determining crystalline structures. XRD can be analyzed in powders and thin films. Crystalline structure of Mn-doped ZnS nanoparticles were analyzed by XRD (Bruker D8 Discover) as shown in Figure 3.12. The condition of XRD used CuKα radiation (λ = 1.5406 Å) at room temperature and scanning rate as 0.02 second per step.

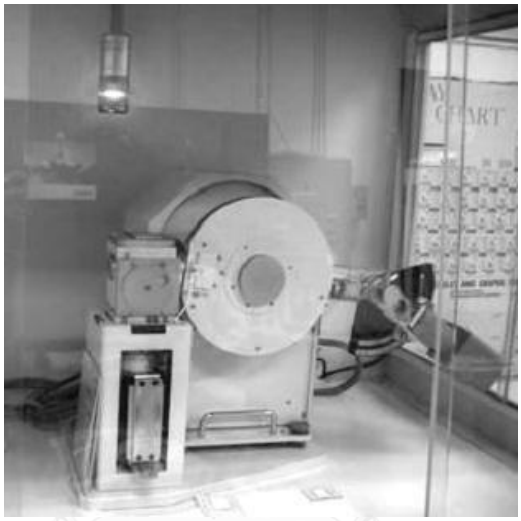

Figure 3.12 X-ray diffractometer (XRD)

3.4.2 Transmission electron microscopy (TEM)

Transmission electron microscopy is a key tool for imaging the internal microstructure of nanoparticles. Crystalline structure could be analyzed by high resolution transmission electron microscopy (HRTEM) and selected area electron diffraction (SAED) mode. All samples were analyzed by using TEM (JEOL-JEM 2100) as shown in Figure 3.13. Mn-doped ZnS nanoparticles were diluted by absolute ethanol. It was dispersed by ultrasonic bath for 1 hour. Dispersing mixture is dropped on a copper grid coated by Formvar film. A grid was loaded into sample chamber and waited vacuum condition and steady state inside the chamber. TEM operated on 120 kV.

Figure 3.13 Transmission electron microscopy (TEM)

3.4.3 Field emission scanning electron microscopy (FE-SEM)

The field emission scanning electron microscopy (FE-SEM: JSM-7001F, Figure 3.14) photograph morphology of particles in microstructure. Mn-doped ZnS nanoparticles were diluted by absolute ethanol. It was dispersed in ultrasonic bath for 1 hour and then dropped on glass slide. The gold nanoparticles were deposited to prevent charging at current 10 mA for 1 minute. The samples were loaded into sample chamber. FE-SEM operated on 20 kV.

Figure 3.14 Field emission scanning electron microscopy (FE-SEM)

3.4.4 Particle size analyzer (Zetasizer)

Particle size analyzer (Zetasizer, nanoseries zen 3600) as shown in Figure 3.15 analyzed particle size distribution. This equipment measured motion of nanoparticles in media such as ethanol or water. The measured particle size is hydrodynamic diameter (D_H). Mn-doped ZnS nanoparticle was diluted and dispersed by absolute ethanol in ultrasonic bath for 1 hour. Then, dispersing mixture loaded into cuvette quartz.

Figure 3.15 Particle size analyzer (Zetasizer)

3.4.5 Spectrofluorometer

Spectrofluorometer (JASCO-FP6200) as illustrated in Figure 3.16 characterized photoluminescence property. Mn-doped ZnS nanoparticle was diluted by absolute ethanol and completely dispersed by ultrasonicate probe. The condition of ultrasonicate probe was 10% of power and sonicated for 2 minutes. Then, colloidal sample was loaded into cuvette quartz for analysis. Spectrofluorometer conditions used excitation wavelength at 280 nm and scanned wavelength in a range 300-700 nm.

Figure 3.16 Spectrofluorometer

3.4.6 X-ray absorption spectroscopy (XAS)

Local structure and oxidation number of samples can be determined by X-ray absorption spectroscopy (Beam line 5.2 SUT-NANOTEC-SLRI) as shown in Figure 3.17. EXAFS and XANES are characterized local structure and oxidation number, respectively. The sample powders are loaded in a slide Kapton as illustrated in Figure 3.17. And then, a Kapton slide was kept in XAS chamber. Higher 5% of concentration in solid solution such as Zn element used transmission mode while lower 5% of concentration in solid solution such as Mn element used fluorescence mode.

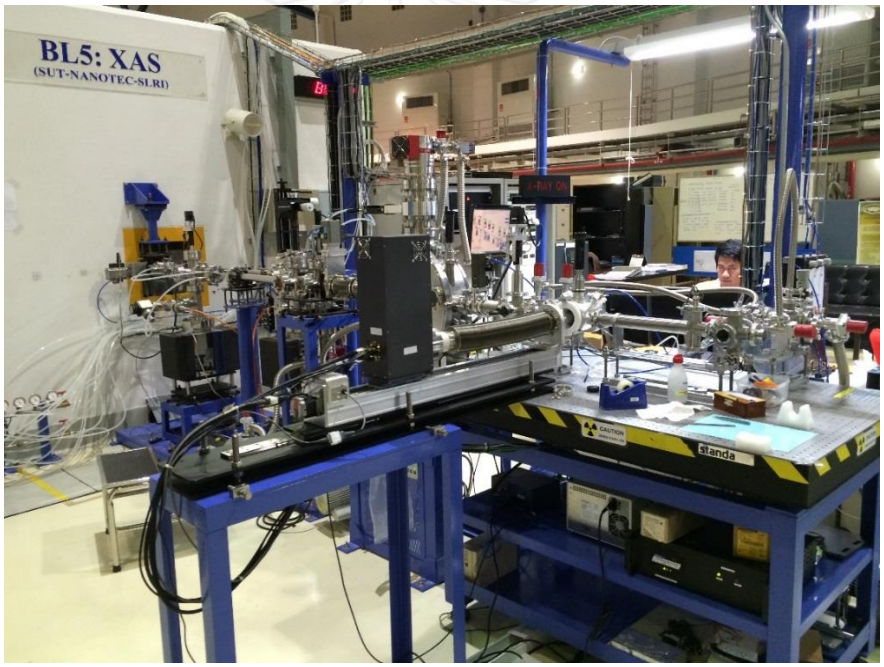

Figure 3.17 X-ray absorption spectroscopy (XAS)

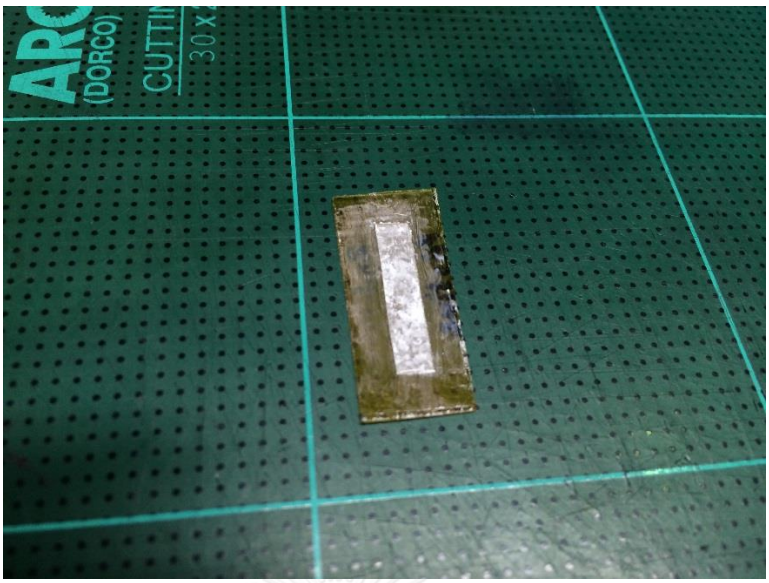

Figure 3.18 Preparation of sample for XAS analysis

CHAPTER IV

RESULTS AND DISCUSSION

4.1 Primary particle size of Mn-doped ZnS nanoparticles at different synthesized method

In this section, we studied the primary particle size of Mn-doped ZnS nanoparticles synthesized by precipitation and micro-emulsion method. Mn-doped ZnS nanoparticles synthesized by precipitation method is easier than micro-emulsion method. Reactant concentrations (C_R) consist of 0.099 molarity (M) of $ZnSO_4$, 0.001 M of $MnSO_4$ and 0.10 M of Na_2S. The molar ratio of water to surfactant (W) is constant. In addition, Mn-doped ZnS nanoparticles synthesized by precipitation method was noted by "PC". In contrast, Mn-doped ZnS nanoparticle synthesized by micro-emulsion method was noted by "ME". The morphology, the primary particle size and crystalline structure of Mn-doped ZnS nanoparticles determined by field emission scanning electron microscopy (FE-SEM) and X-ray diffractometer (XRD), respectively.

In general, the primary particle size of Mn-doped ZnS nanoparticles between synthesized by precipitation method and micro-emulsion method could be analyzed by electron microscope such as scanning electron microscope (SEM) and transmission electron microscope (TEM). In this research, the primary particle size is usually used field emission scanning electron microscope (FE-SEM). However, all particle sizes consist of unequally particle size. Therefore, particle sizes should be described by

a single number. Arithmetic mean or averaged particle size is approximated from the primary particle size of Mn-doped ZnS nanoparticles. The Feret's diameter is a commonly used measurement of particle size that characterized with microscope. The Feret's diameter was defined by "distance between two tangents on opposite sides of the particle" as represented in Figure 4.1.

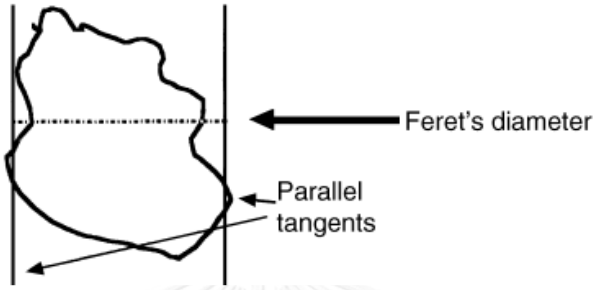

Figure 4.1 Ferret's diameter, reprinting in reference [70]

The orientation of the particle on the microscope slide will affect the projective image. Therefore, particle size was presented by equivalent sphere diameter [70]. The averaged primary particle size (D_p) should be calculated by suitable number of particles [71]. A number of the primary particle sizes can be measured by image-processing program. Dependence of number of particle on the averaged primary particle size of Mn-doped ZnS nanoparticles as W=1 was shown in Figure 4.2. As shown in Figure 4.2, the averaged primary particle size was constant at number of particle ≥ 100. In this work, the number of particle of 200 was chosen for calculating the averaged primary particle size of all samples.

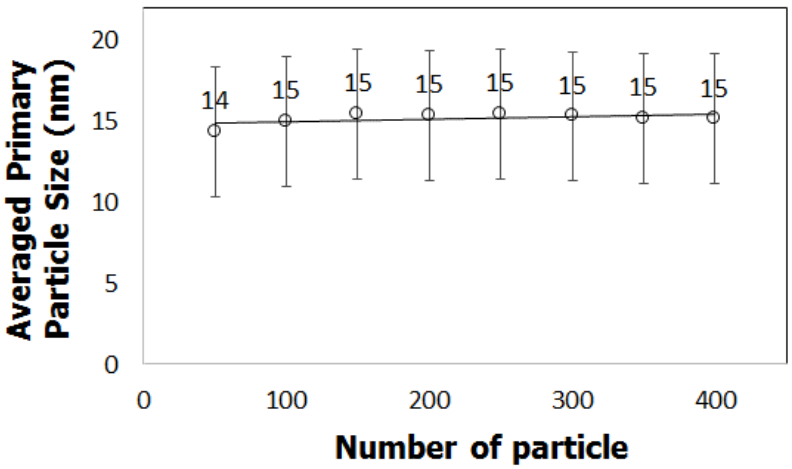

Figure 4.2 Dependence of number of particle on the averaged primary particle size of Mn-doped ZnS nanoparticle synthesized by micro-emulsion at W=1

The morphology of Mn-doped ZnS nanoparticles was analyzed by FE-SEM as shown in Figure 4.3. The agglomeration of the spherically shaped PCs and MEs represented the morphology of these nanoparticles (Figure 4.3 (a-b)). The averaged primary particle size and standard deviation (S.D.) of PC are 103±36 nm. . On the other hand, the averaged primary particle size and standard deviation (S.D.) of ME are 15±4 nm. Figure 4.3 (c) shows particle size distributions of PC and ME. In Figure 4.3 (c), particle size distribution of PC is broader than that of ME. These results are in correspondence with Gan et al. [31]. The cations (Zn^{2+} and Mn^{2+}) and anions (S^{2-}) completely reacted with a result of the larger primary particles of PC. In contrast, micro-emulsion method can control nucleation and growth via the molar ratio of water to surfactant (W) [51,62].

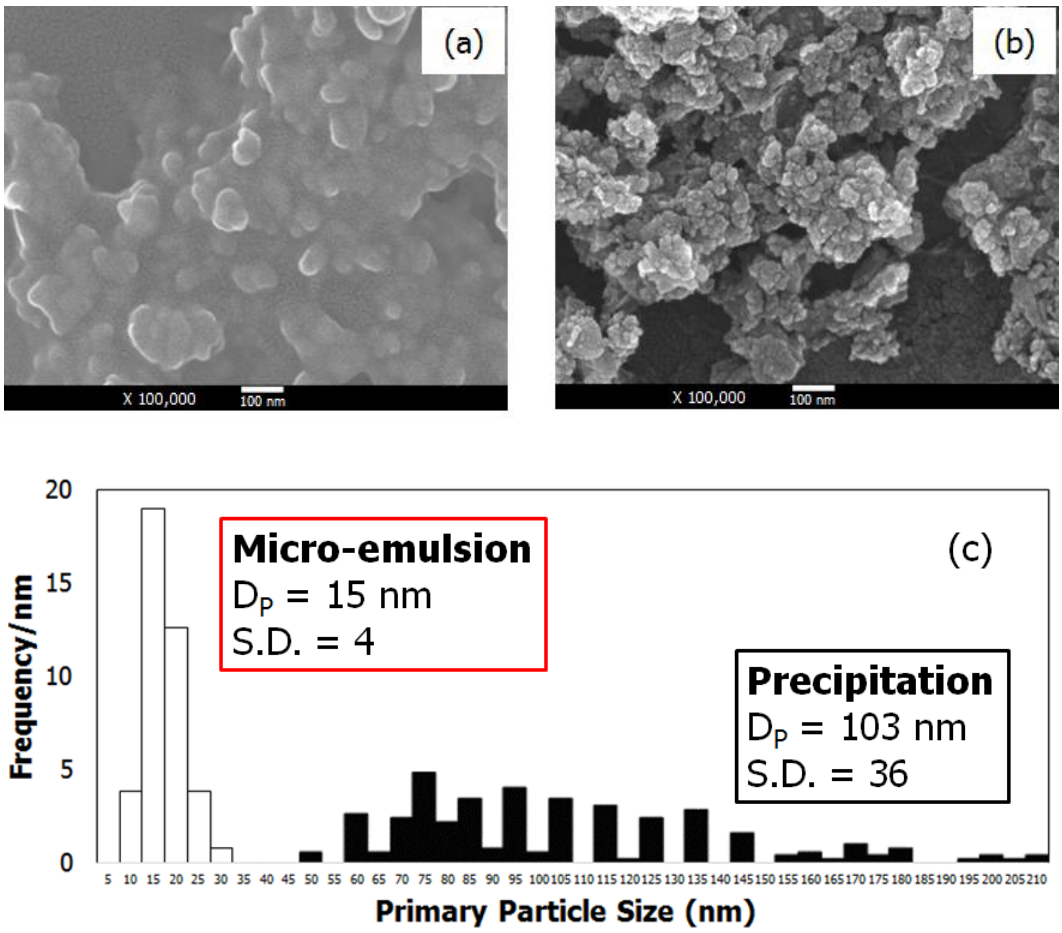

Figure 4.3 FE-SEM images of Mn-doped ZnS nanoparticles synthesized through (a) PC and (b) ME. (c) is particle size distribution of the sample in (a) and (b), respectively.

Crystalline structure of Mn-doped ZnS nanoparticles could be characterized by XRD. Figure 4.4 shows XRD patterns of PC and ME. In Figure 4.4, three peaks at 28.59° (1 1 1), 47.33° (2 2 0) and 56.27° (3 1 1) relatively corresponded to the standard card (JCPDs 01-089-4958). These XRD patterns confirmed zinc blend crystalline structure of Mn-doped ZnS.

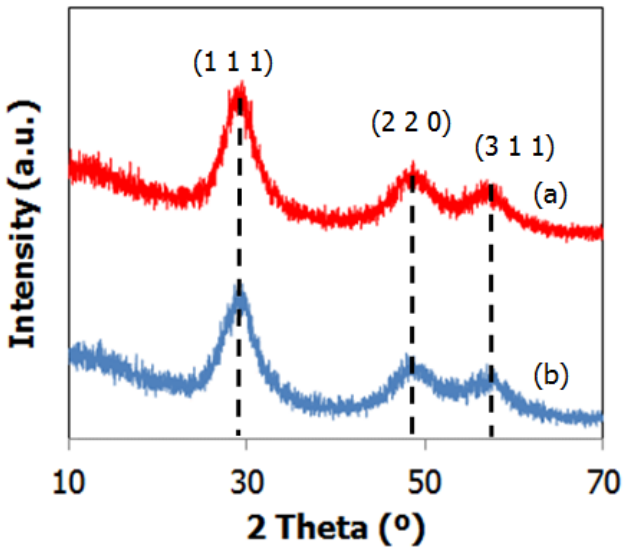

Figure 4.4 XRD patterns of Mn-doped ZnS nanoparticles: (a) precipitation method and (b) micro-emulsion method

As known, many properties of nanoparticle for example optical property depend on the particle size. The smaller sizes of nanoparticles are possibly higher photoluminescent property. Therefore, the Mn-doped ZnS nanoparticles synthesized by micro-emulsion is more appropriate for investigation of the W effect on photoluminescence property in the next section.

4.2 Effect of the molar ratio of water to surfactant on photoluminescence property

Mn-doped ZnS nanoparticles were synthesized by micro-emulsion method. The molar ratio of water to surfactant (W) were varied in a range 1, 3, 5, 7, 11 and 15. Concentration of $ZnSO_4$, $MnSO_4$ and Na_2S were 0.099, 0.001 and 0.10 M, respectively. All experiments were conducted under temperature of 30°C. The morphology, the primary particle size and particle size distribution were determined by

field emission scanning electron microscopy (FE-SEM) and particle size analyser (zetasizer), respectively. Crystalline structures of synthesized Mn-doped nanoparticles were characterized by X-ray diffractometer (XRD), selected area electron diffraction (SAED) and high resolution transmission electron microscopy (HRTEM) while photoluminescence property of Mn-doped ZnS nanoparticles was analysed by spectrofluorometer.

From reaction mechanism in micro-emulsion system as reported in section 3.18, reversed micelle can control nucleation and particle growth because the precipitation occurs inside reversed micelles. Therefore, reversed micelle size can control the final particle size or the primary particle size. The many previous studies explained effect of W values on the final particle size via relationship between the molar ratio of water to surfactant and reversed micelle size. Then, this the effect is explained by the previous studies in the next paragraph.

In 1993, Pileni proposed relationship between the molar ratio of water to surfactant and reversed micelle size. However, reversed micelle sizes are estimated by water pool size in reversed micelles. This relationship was developed as equation 4.1 for assuming spherical reversed micelles as

$$R_D = 3\frac{V_D}{S_D} \tag{4.1}$$

where R_D, V_D and S_D are reversed micelle radius, the volume and the surface area of sphere, respectively. Assuming the volume and the surface area of the droplets are governed by the volume of the water molecules and by the surfactant molecules. Then, assuming water pool radius (R_W) is similar to reversed micelle radius ($R_D = R_W$). It can be expressed in equation 4.2.

$$R_W = 3W\frac{V_{aq}}{A} \quad (4.2)$$

Where R_W, W, V_{aq} and A are water pool radius, the molar ratio of water to surfactant, the volume of water molecule and the polar head area of surfactant, respectively [66]. The volume of water molecule of 30 $Å^3$ was reported by Pileni and colleagues [72], while the polar head area of surfactant of Triton X-100 of 100.7 $Å^2$ was found by Ruiz et al. and Molina-Bolivar et al. [73,74]. Water pool radius were calculated by equation 4.2 with variable W values. Water pool radius were 9, 27, 45, 63, 98 and 134 nm with W=1, 3, 5, 7, 11 and 15, respectively. These dates were plotted in Figure 4.5. In Figure 4.5, the plot between the molar ratio of water to surfactant and water pool radius shows in linear relation. There are the previously various experiments confirmed the linear variation of water pool radius with the molar ratio of water to surfactant as represented in Table 4.1.

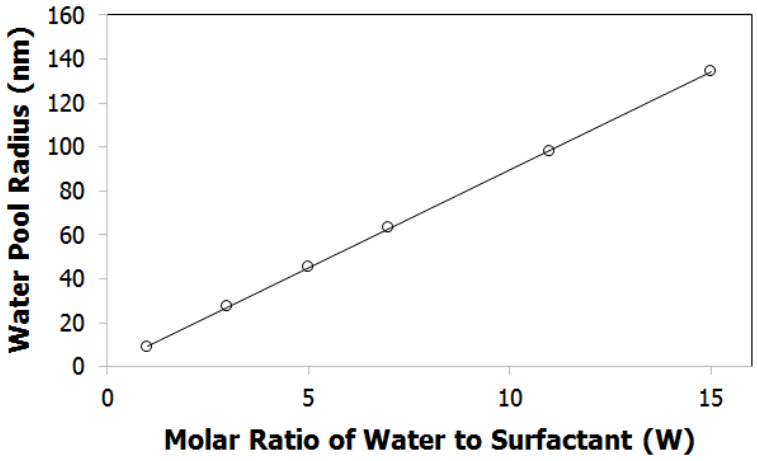

Figure 4.5 Variation of water pool radius of reversed micelle as various W values

Table 4.1 Water pool radius at various W values reported by the previously studies

W	Water pool radius (nm)	Analyzer	Ref.
1-40	100-980	Small angle X-ray scattering (SAXS)	[72]
1.8-8.8	3.7-5.7	Dynamic Quasi Elastic Light Scattering (QELS)	[75]
2-8	1.1-2.3	Small angle X-ray scattering (SAXS)	[76]
5-30	1.4-19.5	Small angle X-ray scattering (SAXS)	[77]
3-60	210-1200	Photon-correlation spectroscopy	[78]
2-15	1.4-4.0	Monte Carlo Simulation	[79]

The morphology and particle size distribution of Mn-doped ZnS nanoparticles at different W values were shown in Figure 4.6. For FE-SEM images, the morphology of Mn-doped ZnS nanoparticles are spherical shape and the primary particles are agglomeration. For particle size distribution as shown in Figure 4.6, particle size distribution is broader as higher W values. In Figure 4.7, the data of the averaged primary particle size and standard deviation of varied W values are 15±4, 19±5, 22±7, 27±6, 31±11 and 35±11, respectively. The averaged primary particle size increases and particle size distribution is broader, when the molar ratio of water to surfactant increases as illustrated in Figure 4.7. These results agreed well with the many previous studies [36,66,75-77,80-87].

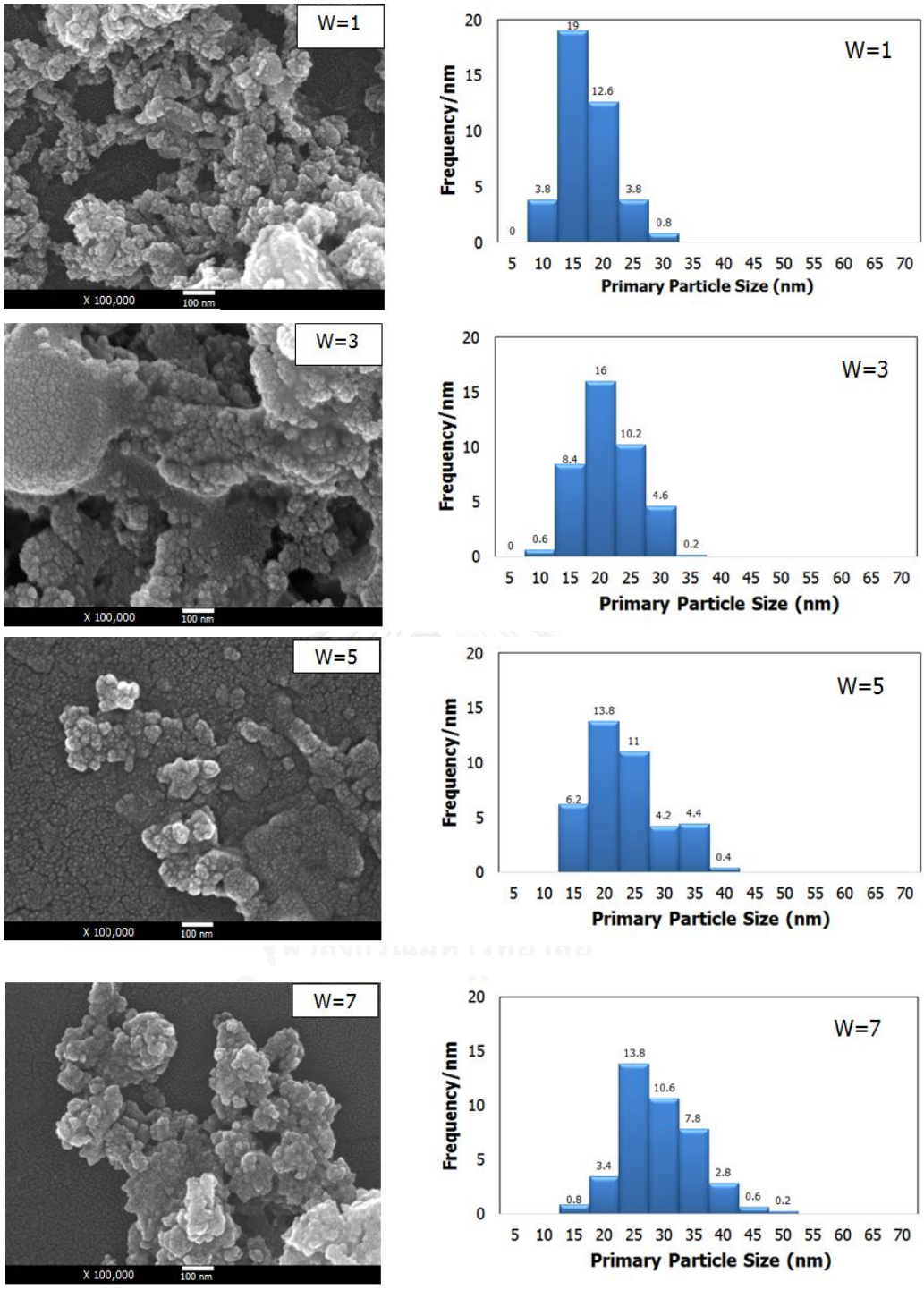

Figure 4.6 FE-SEM images and particle size distribution of Mn-doped ZnS nanoparticles at various W values

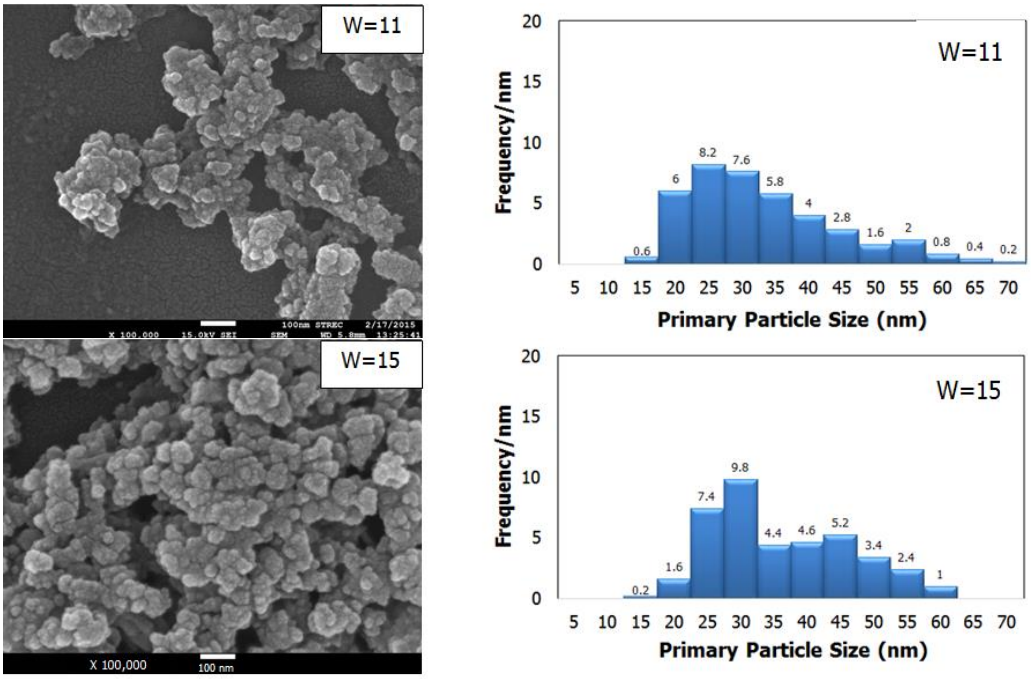

Figure 4.6 FE-SEM images and particle size distribution of Mn-doped ZnS nanoparticles at various W values (Continued)

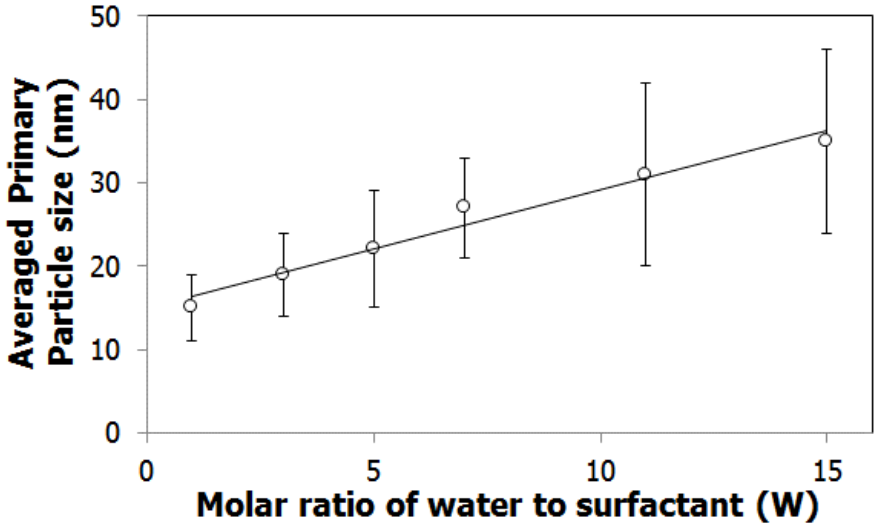

Figure 4.7 Dependence of the molar ratio of water to surfactant on the averaged primary particle sizes analyzed by FE-SEM images

In the many previous studies, explanation of effect of the molar ratio of water to surfactant on the primary particle size consists of mainly two attributions via influence of the molar ratio of water to surfactant on reversed micelle size or water pool size. Firstly, when the W value increases, water pool sizes increases. Therefore, reactant in reversed micelle can exchange by a collision process and possible reaction among reversed micelles to occur more easily. The nucleation rate and particle growth are controlled by the collision, fusion and splitting of reversed micelle. As a result, the averaged primary particle size becomes larger and particle size distribution becomes broaden when W value increases [36,79,80]. Secondary, Qui et al. reported that increase in W value leads to water pool size and number of ions per number of reversed micelle increase [77]. From the nucleation and growth phenomena, the stable nucleus must be formed when ion occupancy number in water pool is much more than the critical number of monomer (N_C) [88]. Then, the nuclei incorporate with ions and it becomes larger particle. Therefore, the higher ratio of number of ions to number of reversed micelle leads to a larger particle size. In summary, with increased W values, the averaged primary particle size of Mn-doped ZnS becomes larger and particle size distribution broader.

On the other hand, the averaged secondary particle size (D_S) was analyzed by zetasizer. The averaged secondary particle sizes were illustrated in Figure 4.8. Dependence of the averaged secondary particle size upon W extracted from all histograms in Figure 4.8 was plotted in Figure 4.9. The averaged secondary particle size and standard deviation of Mn-doped ZnS nanoparticles are 526±138, 315±128, 240±66, 291±85, 244±72 and 340±76 nm at W=1, 3, 5, 7, 11 and 15, respectively. The averaged secondary particle size are larger than the averaged primary particle size because the agglomerated primary particles become the secondary particle as clearly

illustrated FE-SEM images in Figure 4.6. Furthermore, the particle size measured by dynamics light scattering technique was calculated by Stoke-Einstein equation:

$$D_H = \frac{k_B T}{3\pi\eta_V \upsilon} \quad (4.3)$$

where D_H, k_B, T, η_V and υ are hydrodynamic diameter, Boltzmann's constant, absoluted temperature, viscosity and transition diffusion coefficient, respectively [89]. Hydrodynamic diameter is an equivalent diameter of a spherical particle. Thus, the averaged secondary particle size is larger than the averaged primary particle size. In addition, dependence of W on the averaged secondary particle size can be explained by surface per volume of the primary particles. When the primary particle size is smaller, surface area per volume of the primary particle becomes higher. Therefore, the primary particles are more rigorous agglomeration leading to the larger the secondary particle size of nanoparticles [69,90].

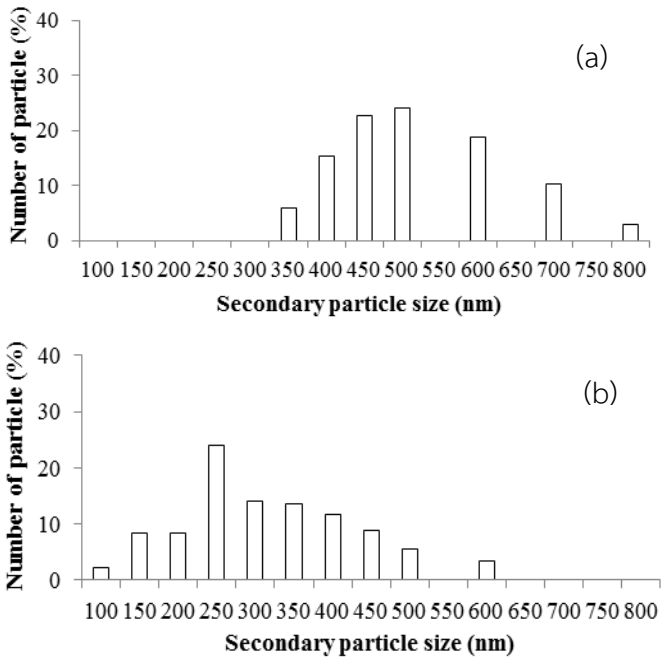

Figure 4.8 Particle size distributions of Mn-doped ZnS nanoparticles: (a) W = 1, (b) W = 3, (c) W = 5, (d) W = 7, (e) W = 11 and (f) W = 15

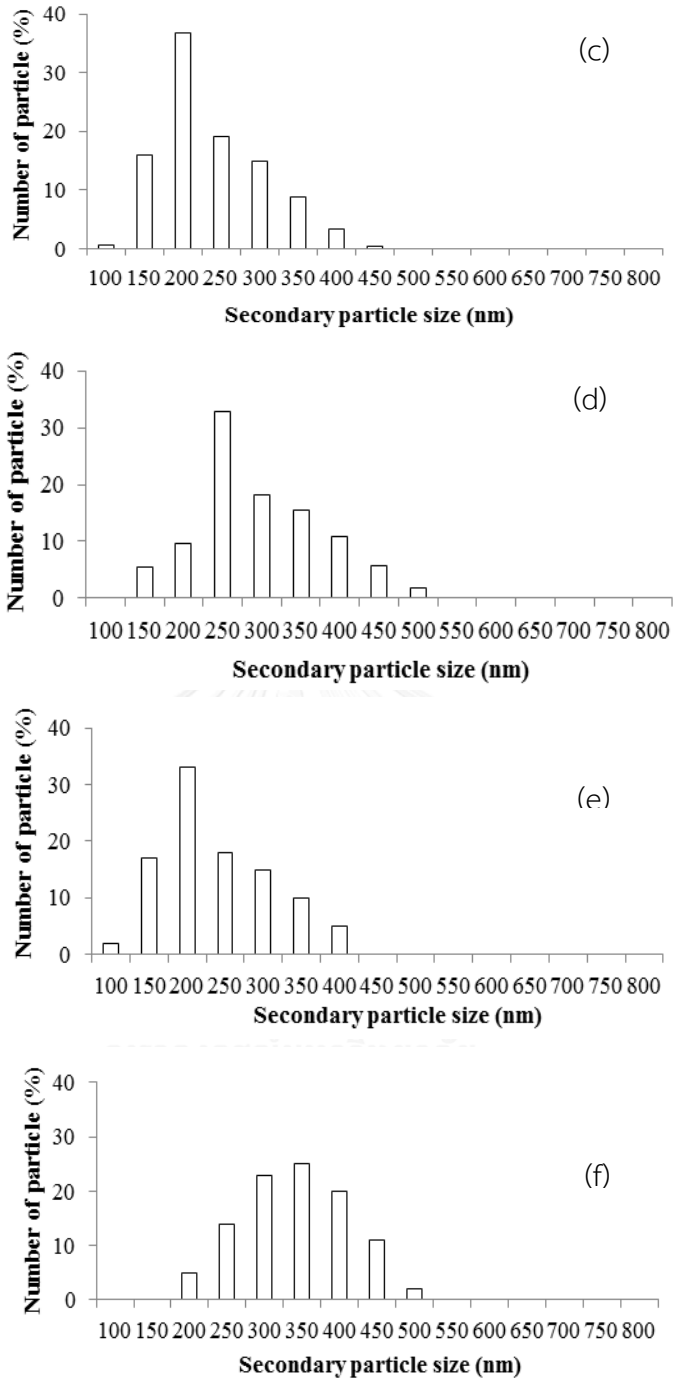

Figure 4.8 Particle size distributions of Mn-doped ZnS nanoparticles: (a) W = 1, (b) W = 3, (c) W = 5, (d) W = 7, (e) W = 11 and (f) W = 15 (Continued)

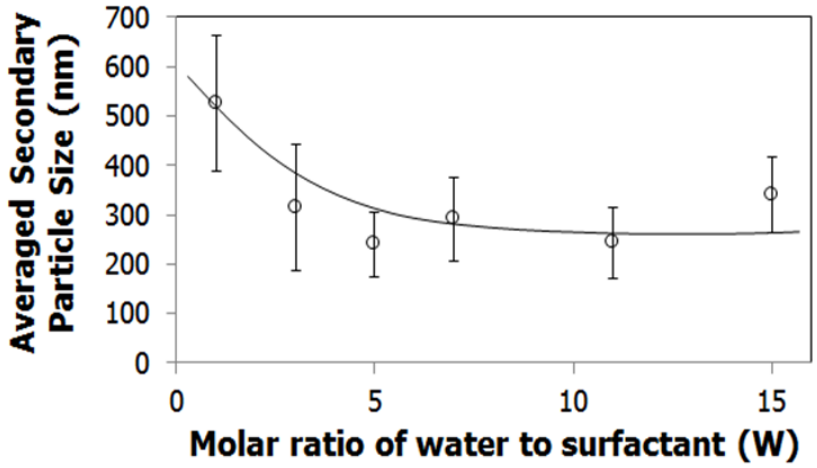

Figure 4.9 Dependence of the molar ratio of water to surfactant on the averaged secondary particle size analysed by zetasizer

XRD patterns of all synthesized samples were shown in Figure 4.10. Three peaks at 29.08° (1 1 1), 48.08° (2 2 0) and 56.52° (3 1 1) are in good agreement with the standard card (JCPDs 01-089-4958), which are also consistent with SAED (discussed later). These XRD patterns reveal that all samples consist of Mn and ZnS crystals which co-exist as the zinc blend crystalline structure. In addition, no crystalline structure of Mn-doped ZnS nanoparticles was changed at various the molar ratios of water to surfactant. Furthermore, the averaged crystalline size (D_C) can be estimated by Scherrer's equation that represented in equation 4.4 where D_C, k, λ, β and θ are the averaged crystalline size, the constant of crystalline sharp factor (~0.90), CuKα radiation wavelength (1.5406 Å), the full width half maximum intensity (FWHM) and Bragg angle of diffraction peak, respectively [91]. FWHM is calculated by the (1 1 1) diffraction peak for all samples.

$$D_C = \frac{k\lambda}{\beta\cos\theta} \tag{4.4}$$

The averaged crystalline sizes were of 2.9, 3.1, 3.2, 3.5, 3.7 and 3.9 nm at the molar ratio of water to surfactant of 1, 3, 5, 7, 11 and 15, respectively. Dependence of the molar ratio of water to surfactant on the averaged crystalline size is plotted in Figure 4.11. The molar ratio of water to surfactant is not significant dependent on the averaged crystalline size.

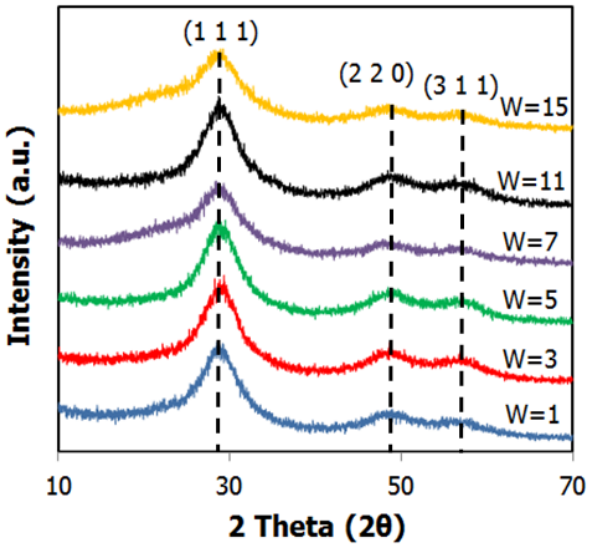

Figure 4.10 XRD patterns of Mn-doped ZnS nanoparticles at various W values

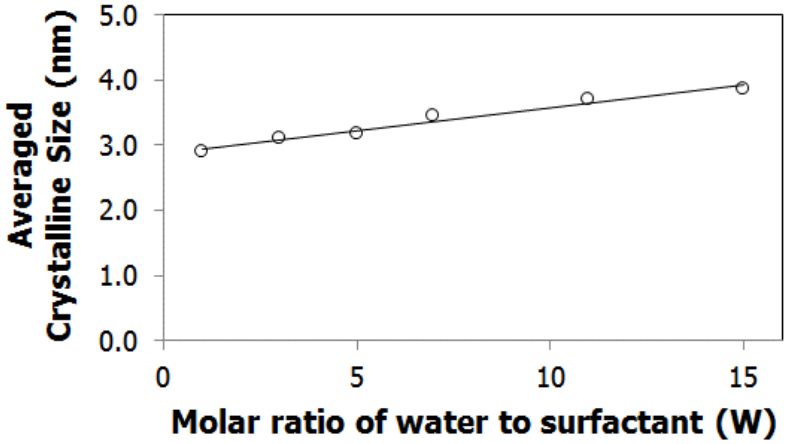

Figure 4.11 Dependence of the molar ratio of water to surfactant on the averaged crystalline size

In addition, the microcrystalline structure of Mn-doped ZnS nanoparticles can be determined by selected area electron diffraction (SAED). SAED patterns of Mn-doped ZnS nanoparticle at various W values were illustrated in Figure 4.12. The Camera equation in Appendix C [92,93] was used to calculate the crystalline planes. The zinc blend crystalline planes (1 1 1), (2 2 0) and (3 1 1) supported the XRD results. In addition, SAED patterns of Mn-doped ZnS nanoparticles are clearly polycrystalline structure according to high resolution transmission electron microscopy (HRTEM) images as shown in Figure 4.13.

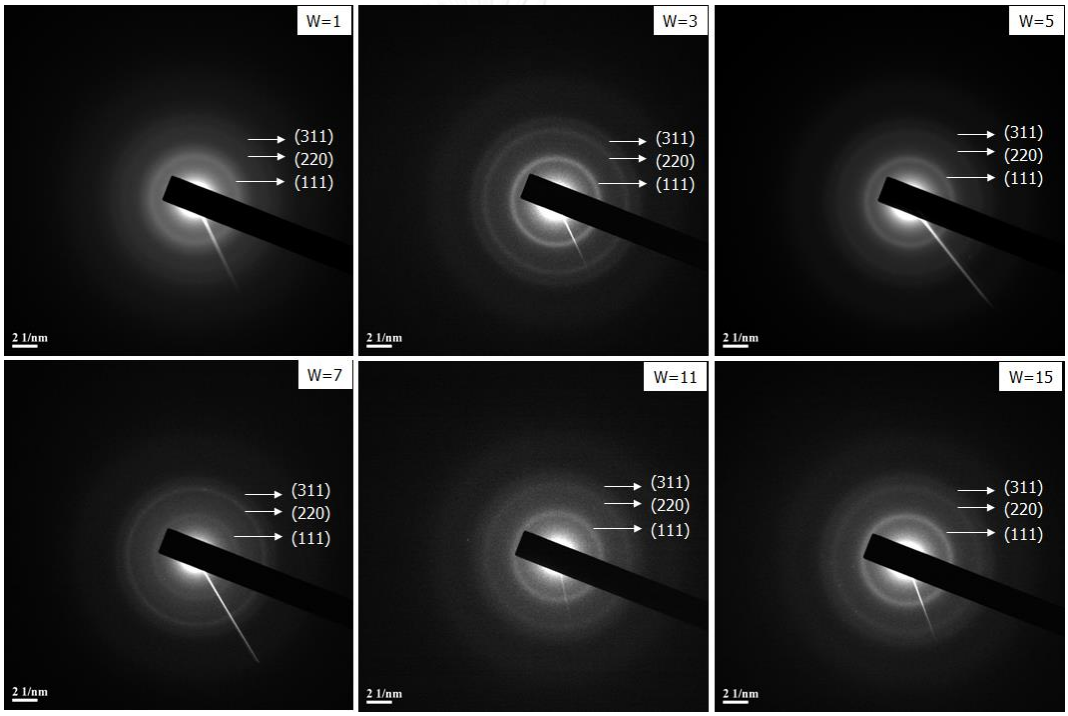

Figure 4.12 SAED images of Mn-doped ZnS nanoparticle at different W values

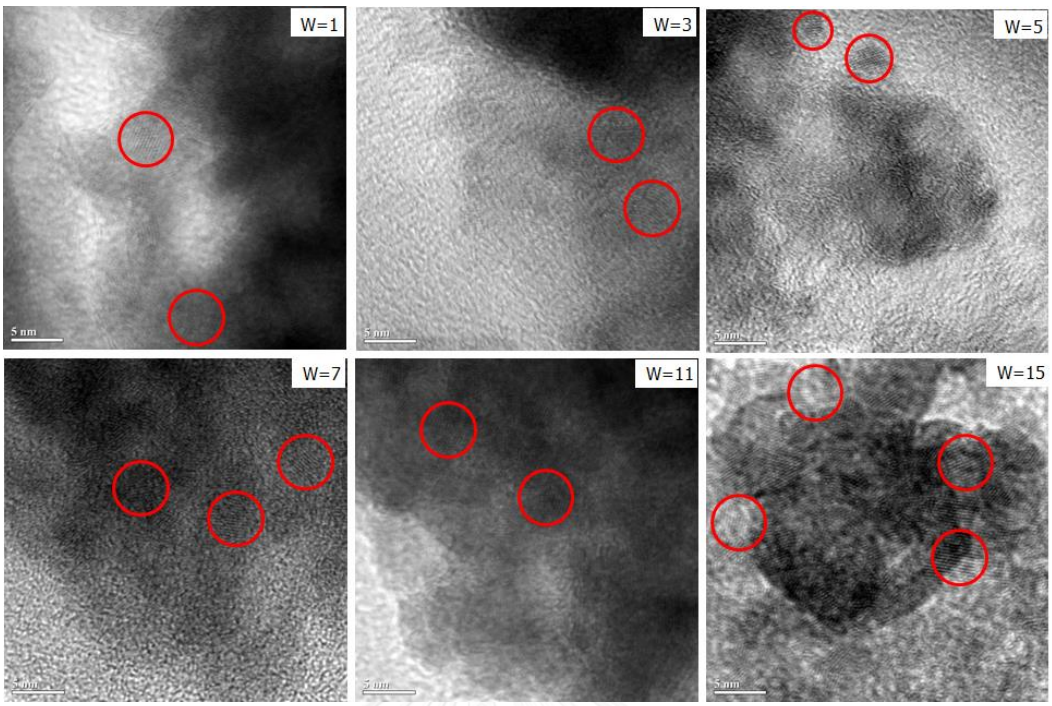

Figure 4.13 HRTEM images of Mn-doped ZnS nanoparticles at different W values

In section 3.17, the molecules can be absorbed by UV light until excited molecules and emitted in visible lights. The emitted visible lights are detected by detector of Spectrofluorometer. The signals from detector are adjusting into graph of intensity versus various wavelengths [94,95]. Therefore, photoluminescence property of Mn-doped ZnS nanoparticles could be determined by Spectrofluorometer.

Photoluminescence property of all synthesized Mn-doped ZnS nanoparticles was observed from Figure 4.14. With W values of 1, 3, 5, 7, 11 and 15, the synthesized Mn-doped nanoparticles exhibited two main peaks which are blue emission peak at 309 nm emitted from ZnS host and another yellow-orange emission at 611 nm emitted from Mn dopant. The energy transfer from s-p states of ZnS host to d-state of Mn metal ions would attribute to emission of yellow-ornange photoluminescence spectra as reported by Bhagawa et al. [29]. In addtion, the emission peak at 340 nm

and 585 nm are emitted by the ZnS vacancies and sulfer vacancies, respectively. These vacancies introduce new energy levels (defect states) in forbidden band gap of semiconductor [48]. The comparision with the emission spectra of Mn-doped ZnS, blue shift about 4 nm of yellow-orange emission were observed. Moreover, ZnS and Mn emission intensity decrease while the relative intensity of Mn emission to ZnS emission almost constant, when the molar ratio of water to surfactant increases as shown in Figure 4.15. Again, higher the molar ratio of water to surfactant leads to smaller the primary particle size. Subsequently, the primary particle size affects to photoluminescence intensity and quantum yield that had been reported by Bhargava et al. and Bhargava [28,29].

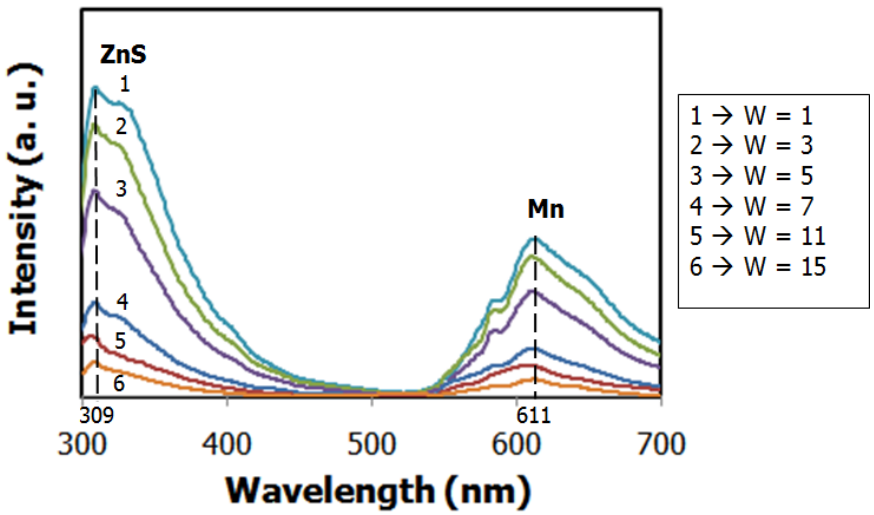

Figure 4.14 Photoluminescence spectrums of Mn-doped ZnS nanoparticles at various W values

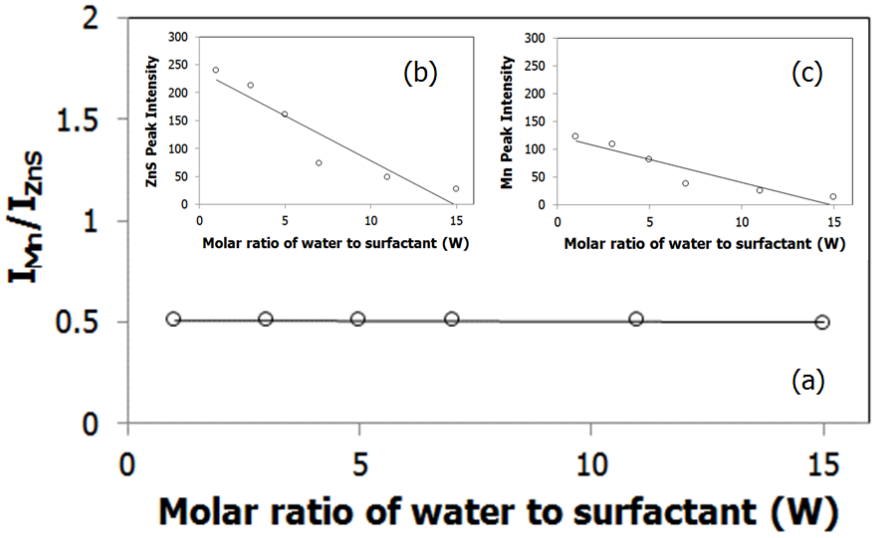

Figure 4.15 Dependence of the molar ratio of water to surfactant on various emission intensities: (a) the relative emission intensity, (b) ZnS emission intensity and (c) Mn emission intensity

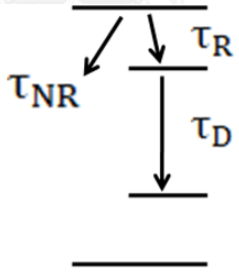

Doping impurity

Figure 4.16 Schematic recombination process in a nanoparticle for doping impurity

In Figure 4.16, after electrons absorbed energy and moved to excited state, the electrons returned to ground state or recombination and emitted energy of light or heat. Therefore, quantum yield is defined by the ratio of radiative recombination rate to total recombination rate as shown in equation 4.6 where η, $1/\tau_R$ and $1/\tau_{NR}$ are quantum yield, radiative rate and non-radiative rate, respectively [96]. Furthermore,

easier definition of quantum yield is the ratio of the number of emitted photons on the number of absorbed photons [58].

$$\eta = \frac{1/\tau_R}{1/\tau_R + 1/\tau_{NR}} \tag{4.6}$$

Non-radiative recombination rate ($1/\tau_{NR}$) should depend on the number of surface atoms per unit volume which inversely proportional to the particles size ($1/D_P$) [97]. The radiative rate of impurity was defined as shown in equation 4.7 where σ, ν_{th} and N are the centre size of an electron, the thermal velocity of an electron and the number of impurities per unit volume, respectively [98].

$$1/\tau_R = \sigma \nu_{th} N \tag{4.7}$$

Assuming there is only impurity per one nanoparticles because concentration quenching of luminescence occur when the doping concentration increases. Thus, the radiative rate ($1/\tau_R$) is proportional to number of density of Mn ion at the Zn site within a nanoparticle. Hence, it is inversely proportional to the volume of the nanoparticle ($1/D_P^3$) for the case of a single Mn ion with in a nanocrystal. The non-radiative recombination rate ($1/\tau_{NR}$) varies as $1/D_P$ as expressed above. Therefore, the expressed quantum yield was shown in equation 4.8 where α is the constant ratio of τ_R to τ_{NR}.

$$\eta = \frac{1}{1 + \alpha D_P^2} \tag{4.8}$$

From equation 4.8, quantum yield increases when the primary particles size deceases [29].

In conclusion, photoluminescence intensity increases when the averaged primary particle size deceases at constant Mn concentration. Moreover, the effect of Mn concentration on photoluminescence property at constant the primary particle size were presented in the next section.

4.3 Effect of Mn concentration on photoluminescence property

In this section, Mn-doped ZnS nanoparticles were synthesized by micro-emulsion method at various Mn concentrations of 0, 6 and 10% by weight. The constant molar ratio of water to surfactant is of 1. All experiments were conducted under room temperature of 30 °C. The morphology and the primary particle size, crystalline structure and photoluminescence property of synthesized Mn-doped nanoparticles were characterized by field emission scanning electron microscopy (FE-SEM), X-ray diffractometer (XRD) and spectrofluorometer. In addition, local structure and oxidation number of Mn-doped ZnS nanoparticles were analysed by extended X-ray absorption fine structure (EXAFS) and X-ray absorption near edge structure (XANES).

The morphology and the averaged primary particle size of nanoparticles determined by FE-SEM were shown in Figure 4.17. The morphology of pristine ZnS nanoparticles, 6% Mn-doped ZnS nanoparticles and 10% Mn-doped ZnS nanoparticles were spherical shape and uniform. The averaged primary particle size of pristine ZnS nanoparticles, 6% weight of Mn-doped ZnS nanoparticles and 10% weight of Mn-doped ZnS nanoparticles were 16±5, 16±6 and 16±5 nm, respectively. Dependence of the averaged primary particle size on Mn concentration is shown in Figure 4.18. This result corresponded with Whiffen et al. who synthesized Mn-doped ZnS nanoparticles by micro-emulsion method at constant W value [48].

Therefore, the averaged primary particle sizes only depend on the molar ratio of water to surfactant as explained in the section 4.2.

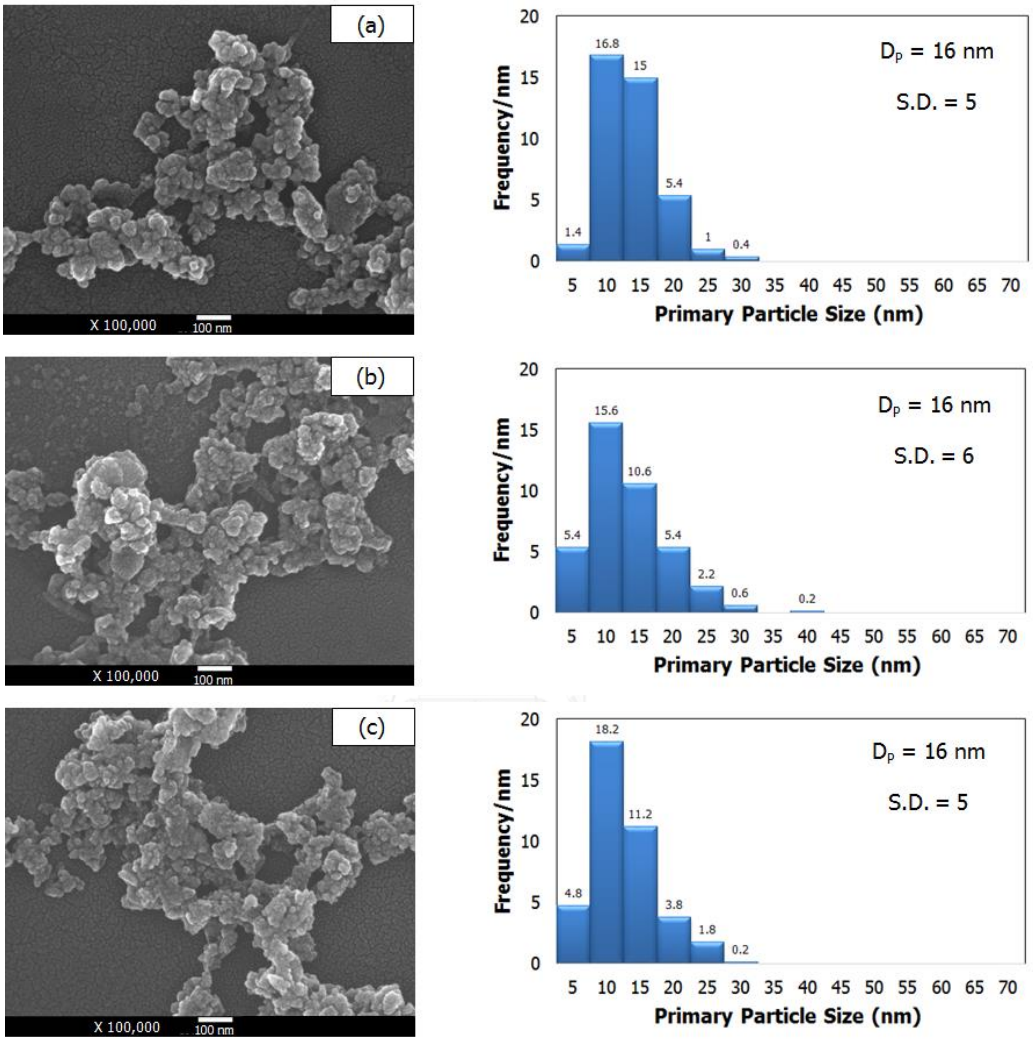

Figure 4.17 FE-SEM images and particle size distribution of Mn-doped ZnS nanoparticles: (a) pristine ZnS, (b) 6% Mn-doped ZnS and (c) 10% Mn-doped ZnS

XRD patterns of synthesized Mn-doped ZnS nanoparticles were represented in Figure 4.18. The three peaks of this nanoparticle appeared at 29.08° (1 1 1), 48.08° (2 2 0) and 56.52° (3 1 1) relative to the standard card (JCPDs 01-089-4958). These XRD patterns reveal that all samples consist of Mn and ZnS crystals which co-exist as

zinc blend crystalline structure. For synthesized pristine ZnS, the XRD pattern was shown in Figure 4.18. Three main peaks at 28.62° (1 1 1), 47.42° (2 2 0) and 56.78° (3 1 1) were confirmed with the standard card (JCPDs 03-065-0309). Inset in Figure 4.18 shows data of (1 1 1) peaks in Gaussian distribution with a range of 20-40°. When Mn concentration increases, (1 1 1) peaks are slightly blue shift. Based on Bragg's equation [91] and Camera equation [92,93], the Bragg angle, d-spacing and lattice parameter values were shown in Table 4.2. When Mn concentration increases, Bragg angle slightly decreases while d-spacing and lattice parameter slightly increase. The Mn^{2+} (ionic radius 0.83 nm [99]) can be incorporated in ZnS lattice. Note that the ionic radius of Zn^{2+} is significantly smaller (0.74 nm). These XRD patterns confirmed the zinc blend crystalline structure and Mn incorporated in ZnS lattice. In addition, Mn concentration had no effect on the crystalline structure of Mn-doped ZnS nanoparticles and no secondary phase was found as confirmed by EXAFS analysis (discussed later).

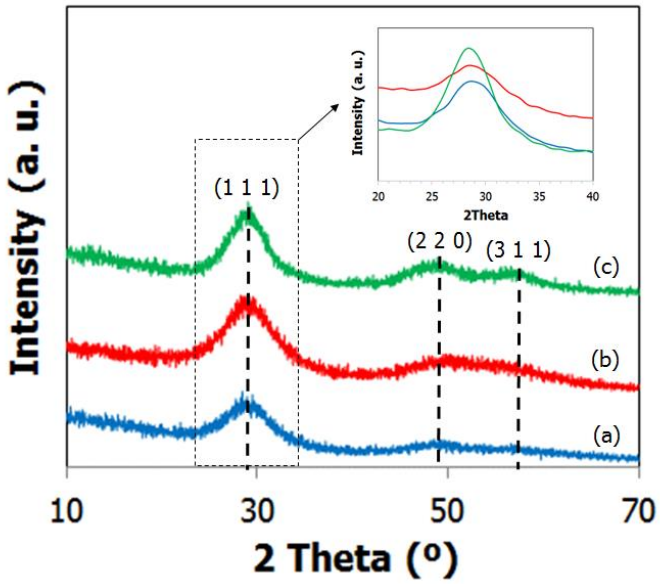

Figure 4.18 XRD patterns of Mn-doped ZnS nanoparticles at various Mn concentrations: (a) pristine ZnS, (b) 6% Mn-doped ZnS and (c) 10% Mn-doped ZnS with the inset showing XRD patterns in a range 20-40°

Table 4.2 Bragg angle, d-spacing and lattice parameter at various Mn concentrations

Mn Concentration (wt. %)	2θ (°)	d-spacing (Å)	Lattice Parameter
0	28.66	3.11176	5.38972
6	28.48	3.13134	5.42363
10	28.41	3.13874	5.43646

The averaged crystalline size of pristine ZnS, 6% Mn-doped ZnS and 10% Mn-doped ZnS are 3.2, 3.3 and 3.4 nm, respectively. The averaged crystalline size at various Mn concentrations was shown in Figure 4.19. The averaged crystalline size of Mn-doped ZnS nanoparticles does not depend on the Mn concentration. Similar results have been previously reported [37,44,48].

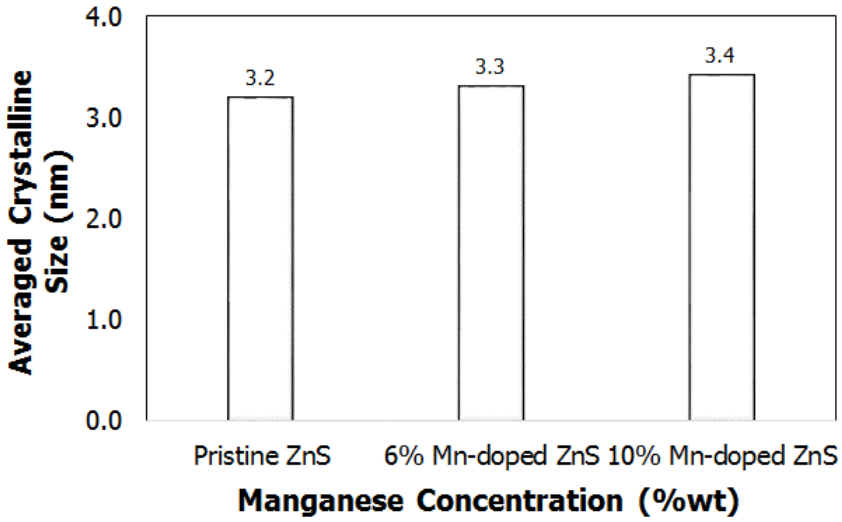

Figure 4.19 Averaged crystalline size at different Mn concentration

Photoluminescence properties of all samples are observed from Figure 4.20. Photoluminescence spectra of Mn-doped ZnS nanoparticles at Mn concentration of 6% and 10% by weight exhibited two main peaks which are blue emission peak at 320 nm emitted from ZnS host and yellow-orange emission peak at 578 nm emitted from doping Mn. Differentially, the photoluminescence spectrum of pristine ZnS was observed at 317 nm as emitted from ZnS host.

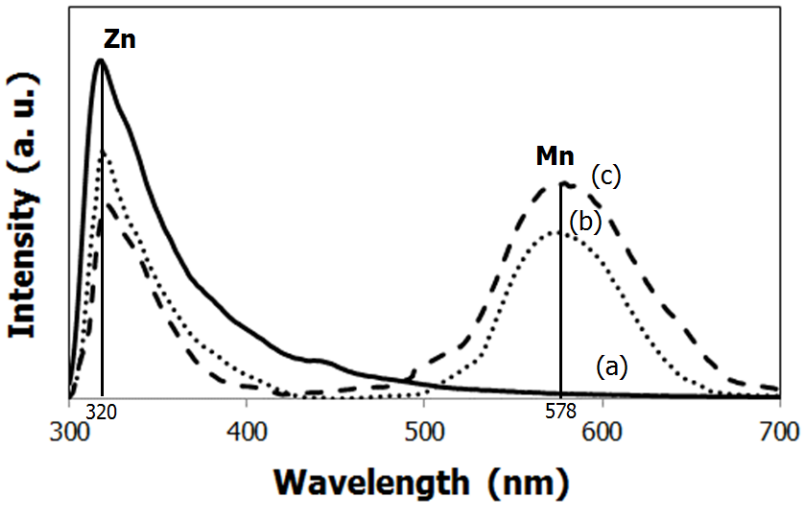

Figure 4.20 Photoluminescence spectrums of Mn-doped ZnS nanoparticles; (a) pristine ZnS, (b) 6% Mn-doped ZnS and (c) 10% Mn-doped ZnS

The photo-physics of undoped and Mn-doped nanocrystals may be explained using schematic diagram in Figure 4.21. In ZnS nanocrystals, the blue emission arises from the de-excitation of ZnS following the energy transfer from the excitation. In Mn-doped nanocrystals, both blue (weak) and yellow-orange (strong) emissions are observed and dominant yellow-orange emission is due to Mn incorporated in ZnS host [38]. In addition, Mn emission intensity shows maximum but ZnS emission intensity shows minimum, when Mn concentration is 10% Mn-doped ZnS. The intensity of yellow-orange emission increases when Mn concentration increases, resulting in

increased the relative intensity of yellow-orange emission to blue emission as shown in Figure 4.22. This result is in correspondence with the previous reports [11,38,39].

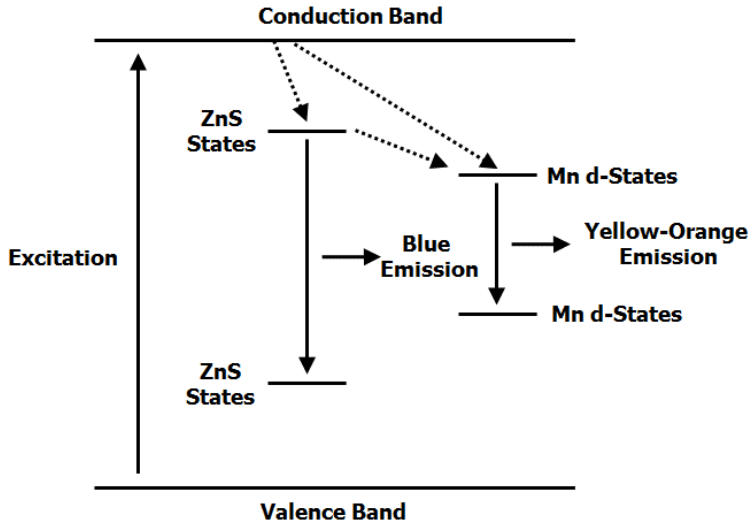

Figure 4.21 Schematic the decay of electron via different channels in Mn-doped ZnS nanocrystals, modified from reference [38]

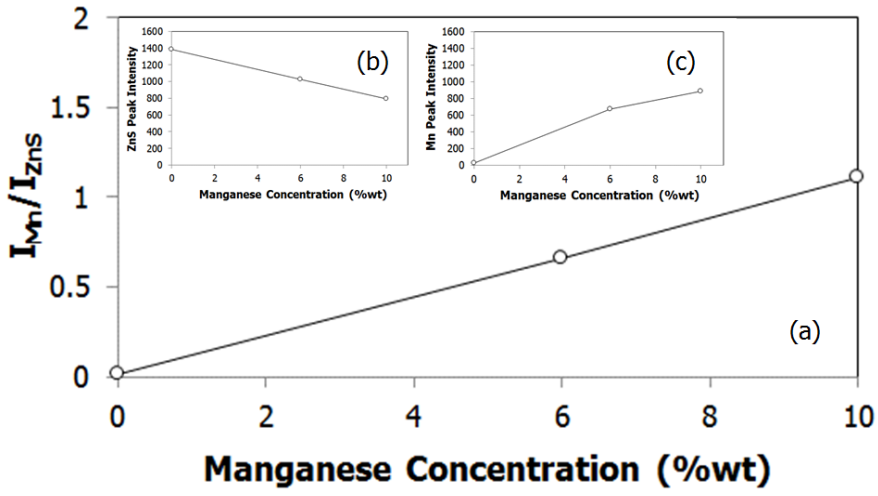

Figure 4.22 Dependence of Mn concentration on various emission intensities: (a) the relative emission intensity, (b) ZnS peak intensity and (c) Mn peak intensity

Furthermore, the position of emission peaks shifts to low energy or redshift of emission peak when the doping concentration increases. This result corresponds with some the previous research [10,21]. Redshift could be explained by the different ion radius between Mn^{2+} and Zn^{2+}. The different ion radius of Mn^{2+} and Zn^{2+} introduce lattice distortion that would influence the energy level structure of ZnS. However, red shift of the yellow-orange emission could be also explained by the high density of surface state [100-102]. The surface area per unit volume for nanoparticles is increased when particle size decrease. Thus, it would bring more defects states on the surface on the surface as increasing Mn concentration.

Substitution of Mn ions in ZnS host can be determined by extended X-ray absorption fine structure (EXAFS) [103,104]. For, pristine ZnS nanoparticles, EXAFS spectra was measured in transmission mode for Zn K-edge. The normalized background and Fourier transformation of the signal of EXAFS data were performed using ATHENA program in the IFEFFIT package [105]. The magnitude of the Fourier transformation of pristine ZnS nanoparticles was shown in Figure 4.23. The radial distance of Zn-S was observed at 2.33 Å in good agreement with EXAFS spectrum of pristine ZnS nanoparticles in Figure 4.23 [106].

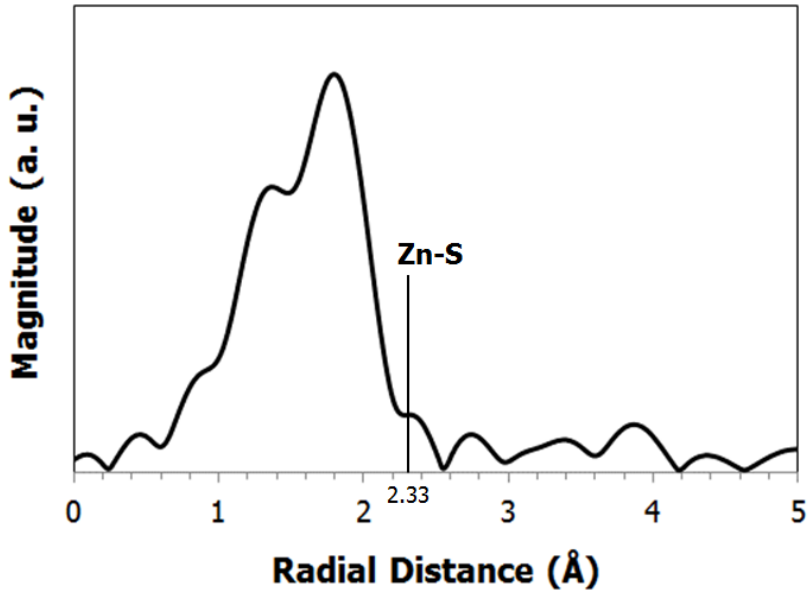

Figure 4.23 Fourier transformed spectra of Zn K-edge EXAFS for pristine ZnS

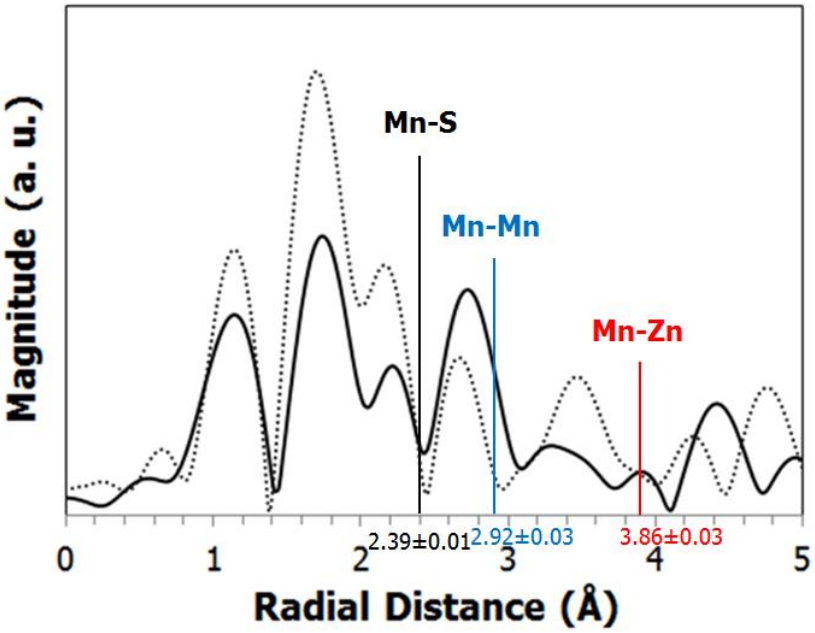

Figure 4.24 Fourier transformed spectra of Mn K-edge EXAFS for Mn-doped ZnS nanoparticles: 6% Mn-doped ZnS (solid line) and 10% Mn-doped ZnS (dot line)

For 6% and 10% Mn-doped ZnS nanoparticles, EXAFS spectrums were measured in fluorescence mode for Mn K-edge. The normalized background and Fourier transformation of measured EXAFS data were also performed using ATHENA program in the IFEFFIT package [105]. When Mn atoms were added in the ZnS host, three types of Mn could be formed: (i) Mn atoms substitutionlly incorporated in ZnS host, (ii) Mn clusters and (iii) Mn sulfide (MnS) compounds. EXAFS spectrums of 6% and 10% Mn-doped ZnS nanoparticles were represented in Figure 4.24. The previous works have been reported that radial distances of Mn-S, Mn-Mn and Mn-Zn were 2.39±0.01 Å, 2.92±0.03 Å and 3.86±0.03 Å, respectively [107,108]. EXAFS peaks of 6% and 10% Mn-doped ZnS nanoparticles presented at ≈3.86 Å, while the two peaks at ≈2.39 Å and ≈2.92 Å were totally disappeared. Therefore, Mn were incorporated in ZnS host, while the Mn clusters and MnS compounds cannot be formed. In addition, these EXAFS results were in agreement with XRD patterns. Unfortunately, many peaks of EXAFS spectra in Figure 4.23 are not correspondent with the radial distance of Zn-S. This is also found in Figure 4.24 that many peaks of EXAFS spectra has no relation with the radial distances of Mn-S, Mn-Mn and Mn-Zn. The point of views should be further investigated.

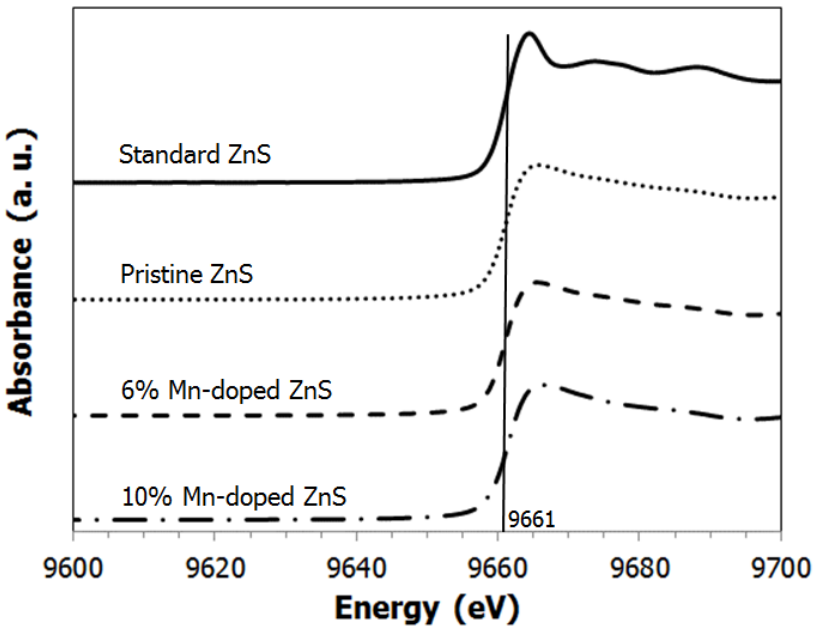

Figure 4.25 Zn K-edge XANES spectrums of Mn-doped ZnS nanoparticles

Oxidation number of Zn and Mn in Mn-doped ZnS nanoparticles could be analyzed by XANES. Figure 4.25 shows the normalized Zn K-edge XANES spectrums of Mn-doped ZnS nanoparticles at various Mn concentrations. For pristine ZnS, 6% and 10% Mn-doped ZnS nanoparticles, the edge energies were found at 9661 eV which is consistent with the edge energy of standard ZnS (oxidation number of Zn = 2+). Therefore, oxidation number of Zn of all samples are also Zn^{2+}. In contrast, Figure 4.26 shows the normalized Mn K-edge XANES spectrums of Mn-doped ZnS nanoparticles at various Mn concentrations. For 6% and 10% Mn-doped ZnS nanoparticles, the edge energy was found at 6548 eV in a relative correspondence with that of standard MnS (oxidation number of Mn = 2+). Therefore, oxidation number of Mn of all samples possesses 2+.

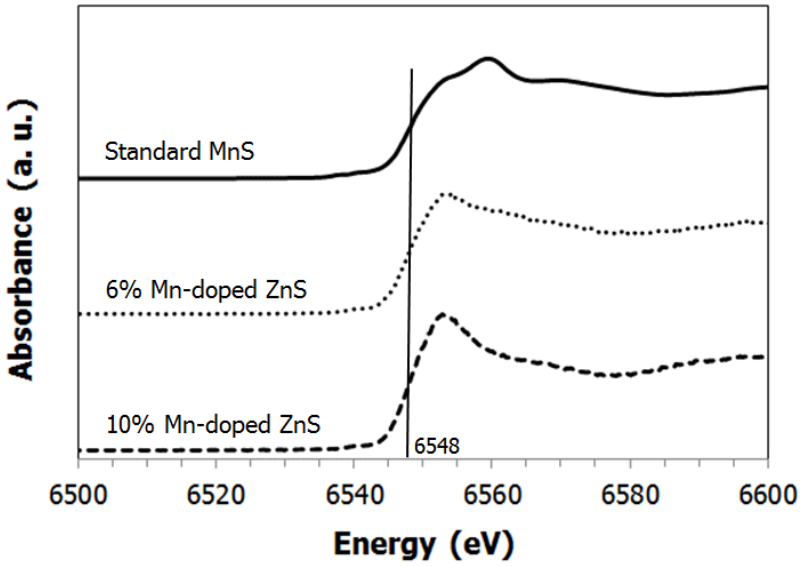

Figure 4.26 Mn K-edge XANES spectrums of Mn-doped ZnS nanoparticles

However, synthesized Mn-doped ZnS nanoparticles at various the molar ratios of water to surfactant and Mn concentration has little amount of product. Increasing reactant concentration is the easiest route for increasing amount of Mn-doped ZnS nanoparticles product. In classical crystallization theory, reactant concentration exactly influences the primary particle size. In addition, the primary particle size also affects photoluminescence property. Therefore, the effect of reactant concentration on the primary particle size will be studied and explained in the next section.

4.4 Effect of reactant concentration on the primary particle size of Mn-doped ZnS nanoparticles

In this section, Mn-doped ZnS nanoparticles were synthesized by micro-emulsion method at various reactant concentrations. The molar ratio of water to surfactant (W) and Mn concentration were fixed at 1 and 6% by weight, respectively. This experiment was varied by reactant concentration as 0.25 and 0.50 M. All synthesized product were conducted under room temperature of 30 °C. The morphology, the primary particle size and crystalline structure of synthesized Mn-doped nanoparticles were characterized by field emission scanning electron microscopy (FE-SEM), X-ray diffractometer (XRD), selected area electron diffraction (SAED) and high resolution transmission electron microscopy (HRTEM), respectively.

From FE-SEM image (Figure 4.27), the morphology of Mn-doped ZnS nanoparticle were spherical shape and uniform. The averaged primary particle size and standard deviation at reactant concentration of 0.25 and 0.50 M are 23±6 and 49±17 nm, respectively. From Figure 4.17 (b), the averaged primary particle size and standard deviation of 0.10 M of reactant concentration is 16±6 nm. Figure 4.28 shows dependence of reactant concentration on the averaged primary particle sizes of Mn-doped ZnS nanoparticles. The averaged primary particle size is larger and particle size distribution is broader, when reactant concentration is higher. These results are in correspondence with the previous studies [77,87,109-111]. In general, the effect of reactant concentration on the primary particle size can be explained by classical crystallization theory. At higher reactant concentration, fast nucleation rate and large number of nucleus were formed. As a result, the primary particle sizes were small [55,90]. In micro-emulsion system, the precipitation was controlled by inter-micellar exchange or mass transfer of reactants. In many the previous studies, many smaller

nuclei size were formed at higher reactant concentration. The nucleus have high surface energy because of small size. Thus, the nuclei aggregate into larger the primary particle size. Meanwhile, aggregation of small nucleus take place via intermicellar exchange leading to larger the primary particles size and broader particle size distribution [77,87,109,110].

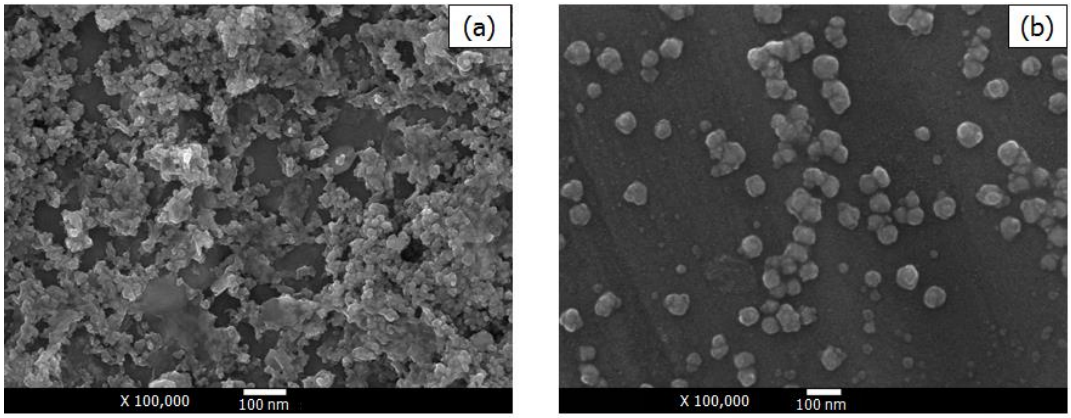

Figure 4.27 FE-SEM images of Mn-doped ZnS nanoparticles synthesized through (a) 0.25 M and (b) 0.50 M. (c) and (d) are the corresponding particle size distribution of the sample in (a) and (b), respectively.

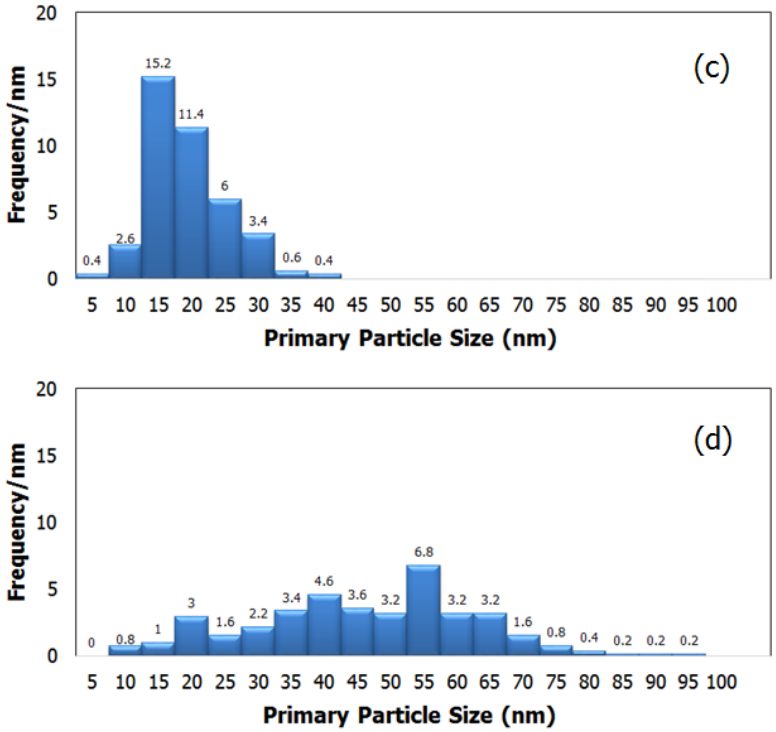

Figure 4.27 FE-SEM images of Mn-doped ZnS nanoparticles synthesized through (a) 0.25 M and (b) 0.50 M. (c) and (d) are the corresponding particle size distribution of the sample in (a) and (b), respectively. (Continued)

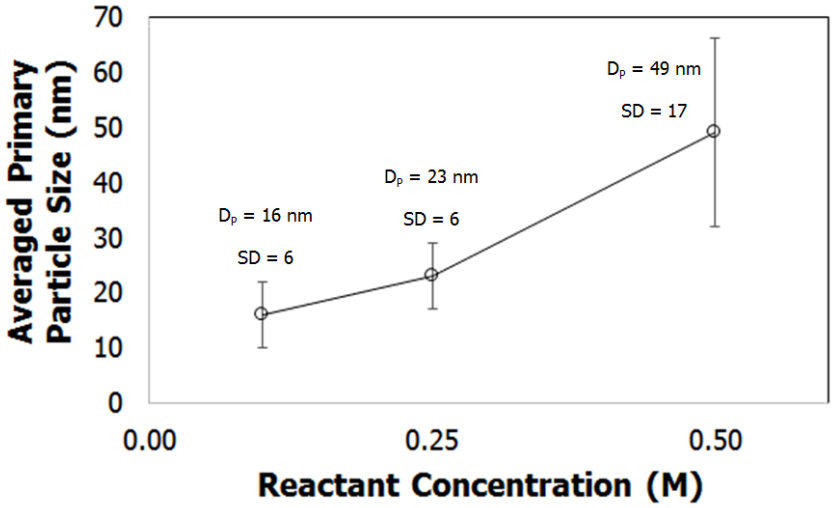

Figure 4.28 Dependence of reactant concentration on the averaged primary particle size of Mn-doped ZnS nanoparticles

XRD patterns of Mn-doped ZnS nanoparticles at reactant concentration of 0.25 and 0.50 M were illustrated in Figure 4.29. The three peaks of this nanoparticle appeared at 29.08° (1 1 1), 48.08° (2 2 0) and 56.52° (3 1 1) relative to the standard card (JCPDs 01-089-4958) which is also consistent with SAED (discussed later). These XRD patterns confirmed that these samples consist of Mn and ZnS crystals which co-exist as zinc blend crystal structure. In addition, the averaged crystalline size at reactant concentration of 0.25 and 0.50 M are 3.5 and 3.9 nm, respectively. Dependence of the averaged crystalline size with reactant concentration is shown in Figure 4.30. Reactant concentration does not significantly depends on the averaged crystalline size of Mn-doped ZnS nanoparticles.

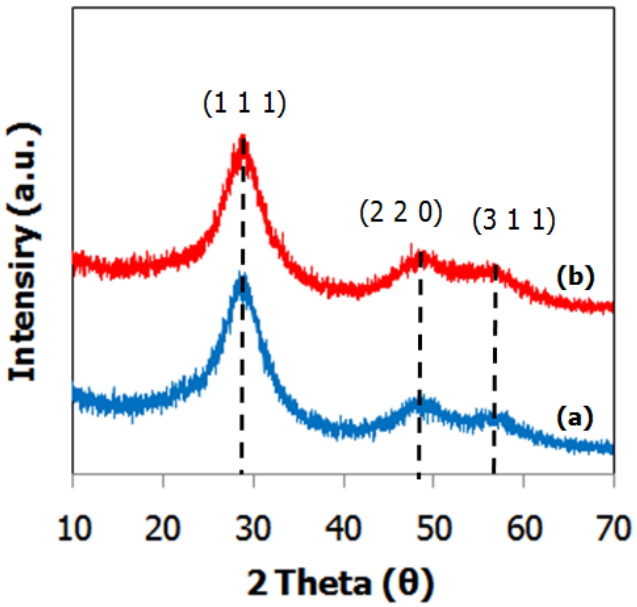

Figure 4.29 XRD patterns of Mn-doped ZnS nanoparticles at various reactant concentrations: (a) 0.25 M and (b) 0.50 M

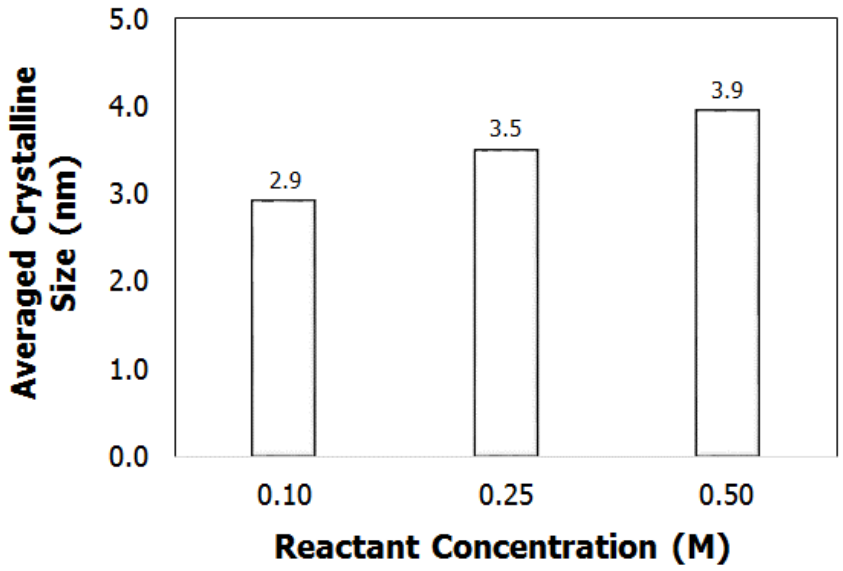

Figure 4.30 Dependence of reactant concentration on the averaged crystalline size

The microcrystalline structure of Mn-doped ZnS nanoparticles were determined by SAED (Figure 4.31). Crystalline planes of Mn-doped ZnS nanoparticle at various reactant concentrations consist of (1 1 1), (2 2 0) and (3 1 1). This result is in a good agreement with XRD patterns. In addition, all synthesized Mn-doped ZnS nanoparticles are polycrystalline structure according to HRTEM images as shown in Figure 4.32.

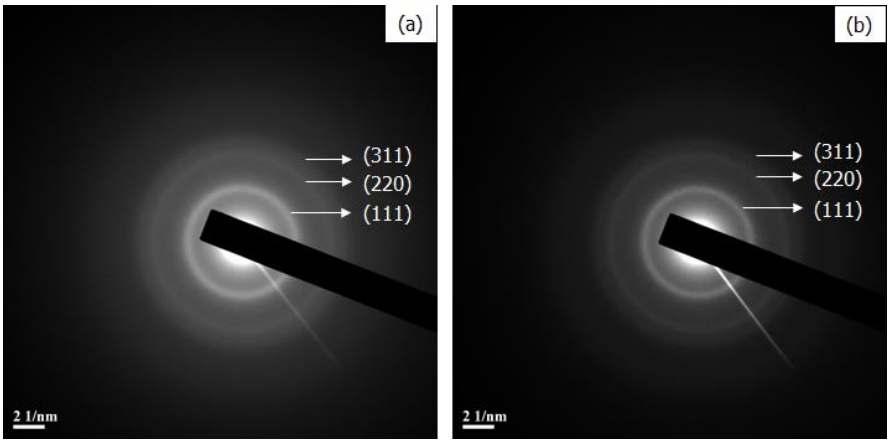

Figure 4.31 SAED images of Mn-doped ZnS nanoparticles at various reactant concentrations: (a) 0.25 M and (b) 0.50 M

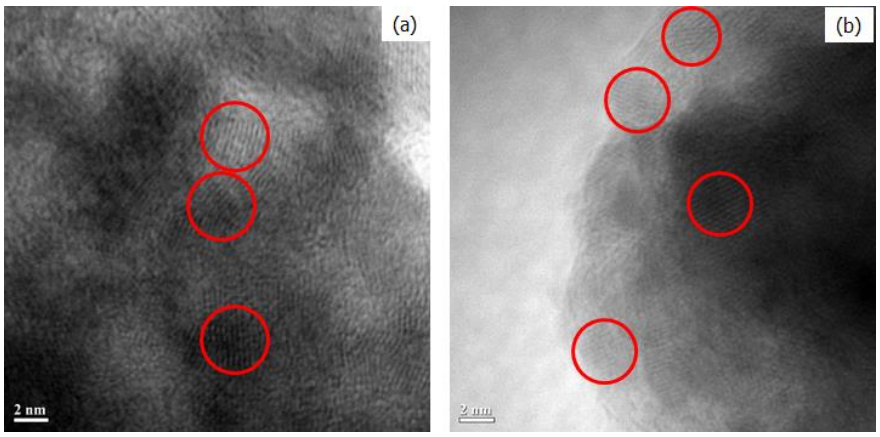

Figure 4.32 HRTEM images of Mn-doped ZnS nanoparticles at various reactant concentrations: (a) 0.25 M and (b) 0.50 M

The amount of Mn-doped ZnS nanoparticles product at various reactant concentrations are shown in Figure 4.33. The amount of product increases when reactant concentration increases. In addition, reaction of synthesized Mn-doped ZnS nanoparticles do not complete when comparison between the amount of product in experimental and the amount of product calculated by theory.

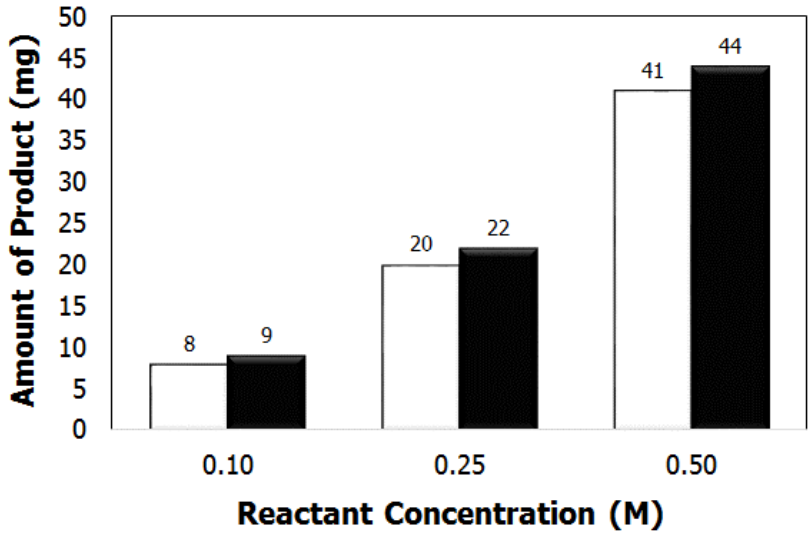

Figure 4.33 Amount of Mn-doped ZnS nanoparticles product at various reactant concentrations: Experiment (White) and Theory (Black)

The amount of Mn-doped ZnS nanoparticles product increases when reactant concentration increases while the averaged primary particle size increases because of aggregation of small nucleus. As a result, decreased photoluminescence property as attributed in section 4.2. However, there is a good idea solving this problem that is synthesis of Mn-doped ZnS nanoparticles with prefabricated micro-emulsion. The total results represented in Appendix F. The morphology and the primary particle size, crystalline structure of Mn-doped ZnS nanoparticles synthesized by prefabricated micro-emulsion were characterized by field emission scanning electron microscopy (FE-SEM), X-ray diffractometer (XRD), selected area electron diffraction (SAED) and high resolution transmission electron microscopy (HRTEM), respectively.

In conclusion, the averaged primary particle size of Mn-doped ZnS nanoparticles is 20±7 nm. XRD pattern and SAED of Mn-doped ZnS nanoparticles are in good agreement with crystalline planes of (1 1 1), (2 2 0) and (3 1 1). Mn-doped ZnS nanoparticles is polycrystalline that was confirmed by SAED and HRTEM images. The amount of product of Mn-doped ZnS nanoparticles synthesized by prefabricated micro-emulsion is higher from 8 to 55 milligrams. It is a very good results because of smaller the primary particle size while higher the amount of product. Unfortunately, these results cannot explanation now but they are interesting in the further investigation.

CHAPTER V

CONCLUSIONS

5.1 Conclusions

The averaged primary particle size of ME is smaller than the averaged primary particle size of PC because the primary particle size of ME was controlled by reversed micelle in micro-emulsion system.

Mn-doped ZnS nanoparticles could be synthesized by micro-emulsion method at various the molar ratio of water to surfactant (W). The morphology of Mn-doped ZnS nanoparticles are spherical shape and the primary particles are agglomeration. The averaged primary particle size of Mn-doped ZnS nanoparticles increases when the molar ratio of water to surfactant increases because of the effect of water pool size in reversed micelle. The averaged secondary particle size increases when the averaged primary particle size decreases because smaller the particle size has high surface energy and agglomerates to larger the averaged secondary particle size. Crystalline structure of all samples was zinc blend crystalline structure that was confirmed by SAED and XRD. SAED and HRTEM images confirmed polycrystalline of Mn-doped ZnS nanoparticles. The emission peak of ZnS and Mn were observed at 309 and 611 nm, respectively. The photoluminescence intensity of ZnS and Mn increases when the averaged primary particle size decreases with explained by quantum yield.

For various Mn concentrations, the averaged primary particle size dose not depend on Mn concentration because of constant the molar ratio of water to surfactant. All synthesized Mn-doped ZnS nanoparticles are zinc blend crystalline structure that was confirm by XRD. The emission peak of pristine ZnS observed at 317 nm while the emission peaks of 6% and 10% Mn-doped ZnS nanoparticles observed blue emission peak at 320 nm emitted from ZnS host and yellow-orange emission peak at 578 nm emitted from Mn. The emission intensity ratio of yellow-orange to blue increases when Mn concentration increases. Mn were incorporated in ZnS host, while the Mn clusters and MnS compounds cannot be formed that were confirmed by EXAFS. In addition, oxidation number of Zn and Mn in Mn-doped ZnS nanoparticles were Zn^{2+} and Mn^{2+}, respectively, which were confirmed by XANES.

For various reactant concentrations, the averaged primary particle size and amount of Mn-doped ZnS nanoparticles product increase when reactant concentration increases. It could be explained by particle growth in micro-emulsion system. SAED and XRD confirmed zinc blend crystalline structure of Mn-doped ZnS nanoparticles. In addition, all synthesized Mn-doped ZnS nanoparticles were polycrystalline that were confirmed by SAED and HRTEM images.

5.2 Expected Benefits

1. Mn-doped ZnS nanoparticles can be synthesized by micro-emulsion method.
2. Understanding effect of W on photoluminescence of ZnS synthesized by micro-emulsion method by taking into account molar ratio of water to surfactant.
3. Understanding effect of Mn on photoluminescence of ZnS synthesized by micro-emulsion method by taking into account Mn concentration.
4. Understanding effect of reactant concentration on the primary particle size of Mn-doped ZnS nanoparticles synthesized by micro-emulsion method.

5.3 Future Works

1. Investigation of Mn-doped ZnS nanoparticles synthesized by prefabricated micro-emulsion as fixed W=1 with increased amount of surfactant and co-surfactant.
2. Application of Mn-doped ZnS nanoparticles in solar concentrator that is prepared by PMMA sheet.

REFERENCES

[1] C.P. Poole, F.J. Owens, Introduction to Nanotechnology, John Wiley & Sons Ice., 2003.

[2] D.W. Deng, J.S. Yu, Y. Pan, Journal of Colloid and Interface Science 299 (2006) 225.

[3] Y. He, H.T. Lu, L.M. Sai, W.Y. Lai, Q.L. Fan, L.H. Wang, W. Huang, Journal of Physical Chemistry B 110 (2006) 13352.

[4] J. Joo, H.B. Na, T. Yu, J.H. Yu, Y.W. Kim, F. Wu, J.Z. Zhang, T. Hyeon, Journal of the American Chemical Society 125 (2003) 11100.

[5] L. Manna, E.C. Scher, A.P. Alivisatos, Journal of the American Chemical Society 122 (2000) 12700.

[6] L. Qu, Z.A. Peng, X. Peng, Nano Letters 1 (2001) 333.

[7] W.W. Yu, X. Peng, Angewandte Chemie - International Edition 41 (2002) 2368.

[8] H. Zhang, L. Wang, H. Xiong, L. Hu, B. Yang, W. Li, Advanced Materials 15 (2003) 1712.

[9] L. Zou, Z. Gu, N. Zhang, Y. Zhang, Z. Fang, W. Zhu, X. Zhong, Journal of Materials Chemistry 18 (2008) 2807.

[10] W.Q. Peng, S.C. Qu, G.W. Cong, X.Q. Zhang, Z.G. Wang, Journal of Crystal Growth 282 (2005) 179.

[11] B. Dong, L. Cao, G. Su, W. Liu, Journal of Colloid and Interface Science 367 (2012) 178.

[12] K. Sooklal, B.S. Cullum, S.M. Angel, C.J. Murphy, Journal of Physical Chemistry 100 (1996) 4551.

[13] K. Barnham, J.L. Marques, J. Hassard, P. O'Brien, Applied Physics Letters 76 (2000) 1197.

[14] J.P. Borah, K.C. Sarma, Acta Physica Polonica A 114 (2008) 713.

[15] M. Dai Prè, I. Morrow, D.J. Martin, M. Mos, A. Del Negro, S. Padovani, A. Martucci, Materials Chemistry and Physics 139 (2013) 531.

[16] M. Shamsipur, H.R. Rajabi, Spectrochimica Acta - Part A: Molecular and Biomolecular Spectroscopy 122 (2014) 260.

[17] W.G.J.H.M. van Sark, G.W. Brandsen, M. Fleuster, M.P. Hekkert, Energy Policy 35 (2007) 3121.

[18] Y. Wada, H. Yin, T. Kitamura, S. Yanagida, Chemical Communications (1998) 2683.

[19] S. Yanagida, H. Kawakami, Y. Midori, H. Kizumoto, C. Pac, Y. Wada, Bulletin of the Chemical Society of Japan 68 (1995) 1811.

[20] A.A. Bol, R. Van Beek, A. Meijerink, Chemistry of Materials 14 (2002) 1121.

[21] S.C. Qu, W.H. Zhou, F.Q. Liu, N.F. Chen, Z.G. Wang, H.Y. Pan, D.P. Yu, Applied Physics Letters 80 (2002) 3605.

[22] L. Sun, C. Yan, C. Liu, C. Liao, D. Li, J. Yu, Journal of Alloys and Compounds 275-277 (1998) 234.

[23] M. Ihara, T. Igarashi, T. Kusunoki, K. Ohno, Journal of the Electrochemical Society 147 (2000) 2355.

[24] R.S. Kane, R.E. Cohen, R. Silbey, Chemistry of Materials 11 (1999) 90.

[25] T. Schmidt, G. Müller, L. Spanhel, K. Kerkel, A. Forchel, Chemistry of Materials 10 (1998) 65.

[26] J. Huang, Y. Yang, S. Xue, B. Yang, S. Liu, J. Shen, Applied Physics Letters 70 (1997) 2335.

[27] W.Q. Peng, G.W. Cong, S.C. Qu, Z.G. Wang, Optical Materials 29 (2006) 313.

[28] R.N. Bhargava, Journal of Luminescence 72-74 (1997) 46.

[29] R.N. Bhargava, D. Gallagher, X. Hong, A. Nurmikko, Physical Review Letters 72 (1994) 416.

[30] J. Cao, J. Yang, Y. Zhang, L. Yang, Y. Wang, M. Wei, Y. Liu, M. Gao, X. Liu, Z. Xie, Journal of Alloys and Compounds 486 (2009) 890.

[31] L.M. Gan, B. Liu, C.H. Chew, S.J. Xu, S.J. Chua, G.L. Loy, G.Q. Xu, Langmuir 13 (1997) 6427.

[32] S.D. Han, K.C. Singh, H.S. Lee, T.Y. Cho, J.P. Hulme, C.H. Han, I.S. Chun, J. Gwak, Materials Chemistry and Physics 112 (2008) 1083.

[33] T.T.Q. Hoa, N.D. The, S. McVitie, N.H. Nam, L.V. Vu, T.D. Canh, N.N. Long, Optical Materials 33 (2011) 308.

[34] H. Hu, W. Zhang, Optical Materials 28 (2006) 536.

[35] C. Jin, J. Yu, L. Sun, K. Dou, S. Hou, J. Zhao, Y. Chen, S. Huang, Journal of Luminescence 66–67 (1995) 315.

[36] G. Murugadoss, Journal of Luminescence 131 (2011) 2216.

[37] S. Nazerdeylami, E. Saievar-Iranizad, Z. Dehghani, M. Molaei, Physica B: Condensed Matter 406 (2011) 108.

[38] S. Sapra, A. Prakash, A. Ghangrekar, N. Periasamy, D.D. Sarma, Journal of Physical Chemistry B 109 (2005) 1663.

[39] R. Sarkar, C.S. Tiwary, P. Kumbhakar, S. Basu, A.K. Mitra, Physica E: Low-Dimensional Systems and Nanostructures 40 (2008) 3115.

[40] B. Steitz, Y. Axmann, H. Hofmann, A. Petri-Fink, Journal of Luminescence 128 (2008) 92.

[41] M. Tanaka, Journal of Luminescence 100 (2002) 163.

[42] B. Tripathi, Y.K. Vijay, S. Wate, F. Singh, D.K. Avasthi, Solid-State Electronics 51 (2007) 59.

[43] S. Ummartyotin, N. Bunnak, J. Juntaro, M. Sain, H. Manuspiya, Solid State Sciences 14 (2012) 299.

[44] Q. Xiao, C. Xiao, Applied Surface Science 254 (2008) 6432.

[45] H. Yang, S. Santra, P.H. Holloway, Journal of Nanoscience and Nanotechnology 5 (2005) 1364.

[46] H. Yang, Z. Wang, M. Zhao, J. Wang, D. Han, H. Luo, L. Wang, Materials Chemistry and Physics 48 (1997) 60.

[47] X.B. Yu, L.H. Mao, F. Zhang, L.Z. Yang, S.P. Yang, Materials Letters 58 (2004) 3661.

[48] R.M. Krsmanović Whiffen, D.J. Jovanović, Z. Antić, B. Bártová, D. Milivojević, M.D. Dramićanin, M.G. Brik, Journal of Luminescence 146 (2014) 133.

[49] S.W. Lu, B.I. Lee, Z.L. Wang, W. Tong, B.K. Wagner, W. Park, C.J. Summers, Journal of Luminescence 92 (2000) 73.

[50] L. Brus, Journal Quantum Electronics 22 (1986) 1909.

[51] J. Eastoe, M.J. Hollamby, L. Hudson, Advances in Colloid and Interface Science 128-130 (2006) 5.

[52] T. Charinpanitkul, A. Chanagul, J. Dutta, U. Rungsardthong, W. Tanthapanichakoon, Science and Technology of Advanced Materials 6 (2005) 266.

[53] J. Xu, Y. Li, Journal of Colloid and Interface Science 259 (2003) 275.

[54] C. Smith, A.R. Barron, 2015.

[55] W.D. Callister, D.G. Rethwish, Material Science and Engineering: an Introduction, John Wiley & Son Inc., 2009.

[56] R.J.D. Miller, G.L. McLendon, A.J. Nosik, W.S.F. Willig, Surface Electron Transfer Processes, VCH Publisher Inc., 1995.

[57] 2015.

[58] B. Valeur, M.N. Berberan-Santos, Molecular Fluorescence; Principles and Applications, Wiley-VCH Verlag & Co. KGaA, Germany, 2013.

[59] T.P. Hoar, J.H. Schulman, Nature 152 (1943) 102.

[60] J.H. Schulman, W. Stoeckenius, L.M. Prince, Journal of Physical Chemistry 63 (1959) 1677.

[61] P.A. Winsor, Transactions of the Faraday Society 44 (1948) 376.

[62] M. Fanan, Microemulsion: Properties and Applications, CRC Press, New York, 2009.

[63] I. Capek, Advances in Colloid and Interface Science 110 (2004) 49.

[64] R. Nagarajan, Langmuir 1 (1985) 331.

[65] D.J. Mitchell, B.W. Ninham, Journal of the Chemical Society, Faraday Transactions 2: Molecular and Chemical Physics 77 (1981) 601.

[66] M.P. Pileni, Journal of Physical Chemistry 97 (1993) 6961.

[67] A.S. Bommarius, J.F. Holzwarth, D.I.C. Wang, T.A. Hatton, Journal of Physical Chemistry 94 (1990) 7232.

[68] P.D.I. Fletcher, A.M. Howe, B.H. Robinson, Journal of the Chemical Society, Faraday Transactions 1: Physical Chemistry in Condensed Phases 83 (1987) 985.

[69] A.D. Randolph, M.A. Larson, Theory of Particulate Processes; Analysis and Techniques of Continuous Crystallization, Acadamic Press InC., London, 1988.

[70] M. Rhodes, Introduction to Particle Technology, John Wiley & Sons Inc., 2008.

[71] W.C. Hinds, Aerosol Technology: Properties, Behavior and Measurment of Airborne Particles, John Wiley & Son Inc., 1999.

[72] M.P. Pileni, T. Zemb, C. Petit, Chemical Physics Letters 118 (1985) 414.

[73] C. Carnero Ruiz, J.A. Molina-Bolívar, J. Aguiar, G. MacIsaac, S. Moroze, R. Palepu, Langmuir 17 (2001) 6831.

[74] J.A. Molina-Bolívar, J. Aguiar, C. Carnero Ruiz, Journal of Physical Chemistry B 106 (2002) 870.

[75] A. Nanni, L. Dei, Langmuir 19 (2003) 933.

[76] K. Kimijima, T. Sugimoto, Journal of Colloid and Interface Science 286 (2005) 520.

[77] S. Qiu, J. Dong, G. Chen, Journal of Colloid and Interface Science 216 (1999) 230.

[78] M. Zulauf, H.F. Eicke, Journal of Physical Chemistry 83 (1979) 480.

[79] M. Ethayaraja, K. Dutta, D. Muthukumaran, R. Bandyopadhyaya, Langmuir 23 (2007) 3418.

[80] R.P. Bagwe, K.C. Khilar, Langmuir 13 (1997) 6432.

[81] J.L. Lemyre, A.M. Ritcey, Chemistry of Materials 17 (2005) 3040.

[82] Y. Li, X. He, M. Cao, Materials Research Bulletin 43 (2008) 3100.

[83] I. Lisiecki, M.P. Pileni, Journal of the American Chemical Society 115 (1993) 3887.

[84] I. Lisiecki, M.P. Pileni, Journal of Physical Chemistry 99 (1995) 5077.

[85] D. Makovec, A. Košak, A. Žnidaršič, M. Drofenik, Journal of Magnetism and Magnetic Materials 289 (2005) 32.

[86] M.P. Pileni, Langmuir 13 (1997) 3266.

[87] S. Qiu, J. Dong, G. Chen, Powder Technology 113 (2000) 9.

[88] T.F. Towey, A. Khan-Lodhi, B.H. Robinson, Journal of the Chemical Society, Faraday Transactions 86 (1990) 3757.

[89] P. Becher, Emulsions Theory and Practice, American Chemical Society, 2001.

[90] A. Mersmann, Crystallization Technology Handbook, Marcel Dekker Inc., USA, 2001.

[91] D.J. Dyson, X-ray and Electron Diffaction Studies in Materials Science, Maney Publishing, London, 2004.

[92] B. Fultz, J. Howe, Transmission Electron Microscopy and Diffractometry of Materials, Springer-Verlag, 2013.

[93] บ. เงาถาวรชัย, หลักการเบื้องต้นกล้องจุลทรรศน์อิเล็กตรอนชนิดส่องผ่านสำหรับงานวัสดุศาสตร์, โรงพิมพ์เลี่ยงเชียง, ประเทศไทย, 2008.

[94] J.R. Lakowicz, Principles of Fluorescence Spectroscopy, Springer Science Business Media LLC, Singapore, 2006.

[95] ล. ศรีพงศ์, การวิเคราะห์เชิงฟลูออโรเมตรี, คณะเภสัชศาสตร์ มหาวิทยาลัยศิลปากร, ประเทศไทย, 2001.

[96] N.H. Jr., Solid State Physical Electronics Series, Prentice-Hell Inc., New Jersey, 1971.

[97] Y. Kayanuma, Physical Review B 38 (1988) 9797.

[98] C.M. Wolfe, N.H. Jr., G.E. Stillman, Physical Properties of Semiconductors, Prentice-Hell Inc., New Jersey, 1989.

[99] R.D. Shannon, Acta Crystallographica Section A 32 (1976) 751.

[100] N. Karar, S. Raj, F. Singh, Journal of Crystal Growth 268 (2004) 585.

[101] N. Karar, F. Singh, B.R. Mehta, Journal of Applied Physics 95 (2004) 656.

[102] Z. Ren, H. Yang, L. Shen, S.D. Han, Journal of Materials Science: Materials in Electronics 19 (2008) 1.

[103] D.C. Koningsberger, R. Prins, X-ray Absorption: Principles, Applications, Techniques of EXAFS, SEXAFS, and XANES, John Wiley & Son Inc., 1988.

[104] ว. คล้ายสุบรรณ์, เทคนิคการทดลอง X-ray Absorption Spectroscopy ณ ห้องปฏิบัติการแสงสยาม, บริษัท สมบูรณ์การพิมพ์ จำกัด, ประเทศไทย, 2012.

[105] M. Newville, Journal of Synchrotron Radiation 8 (2001) 322.

[106] J.S. Jang, S.H. Choi, E.S. Kim, J.S. Lee, N. Shin, D.R. Lee, Chemical Physics Letters 468 (2009) 253.

[107] K. ŁAwniczak-Jabłonska, R.J. Iwanowski, Z. Gołacki, A. Traverse, S. Pizzini, A. Fontaine, I. Winter, J. Hormes, Physical Review B - Condensed Matter and Materials Physics 53 (1996) 1119.

[108] Y.L. Soo, Z.H. Ming, S.W. Huang, Y.H. Kao, R.N. Bhargava, D. Gallagher, Physical Review B 50 (1994) 7602.

[109] M. de Dios, F. Barroso, C. Tojo, M.A. López-Quintela, Journal of Colloid and Interface Science 333 (2009) 741.

[110] L.M. Gan, K. Zhang, C.H. Chew, Colloids and Surfaces A: Physicochemical and Engineering Aspects 110 (1996) 199.

[111] C.Y. Tai, M.H. Lee, Y.C. Wu, Chemical Engineering Science 56 (2001) 2389.

APPENDICES

APPENDIX A

NOMENCLATURE

a	=	lattice parameter
A	=	the polar head area of surfactant
A_1	=	atomic weight of element 1
ΔA	=	change in interfacial area
CMC	=	critical micelle concentration
C_1	=	concentration of element 1 by weight percent
C_1'	=	concentration of element 1 by mole percent
C_{Mn}	=	Mn concentration
C_R	=	reactant concentration
DOS	=	density of electronic state
D_C	=	the averaged crystalline size
D_H	=	hydrodynamic diameter
D_P	=	the averaged primary particle size
D_S	=	the averaged secondary particle size
d_{SAED}	=	d-spacing calculated by SAED pattern
E_f	=	fermi energy
E_g	=	band gap energy
ΔG	=	Gibbs free energy change
ΔH	=	enthalpy change
I_{Mn}/I_{ZnS}	=	the relative emission intensity
i	=	empirical exponent

k	=	the constant of crystal shape factor (~0.90)
k_B	=	Boltzmann's constant
L	=	the fully extended chain length of the surfactant
L_C	=	camera length
l	=	bar length in SAED image
m_1	=	the weight or mass of elements 1
m_2	=	the weight or mass of elements 2
N	=	the number of impurities per unit volume
N_C	=	the critical number of monomer
n	=	number on bar in SAED image
n_{m1}	=	the number of mole in element 1
n_{m1}	=	the number of mole in element 2
P	=	pressure
R	=	the radius of reversed micelle
R_C	=	radius of crystal plane
R_D	=	the radius of sphere droplet
r	=	nucleus radius
r_c	=	critical nucleus radius
SD	=	standard deviation
S_D	=	the surface area of sphere
ΔS	=	entropy change
T	=	temperature (K)
V	=	the surfactant hydrocarbon volume
V_D	=	the volume of sphere droplet
V_{aq}	=	the volume of water molecule
W	=	the molar ratio of water to surfactant
x	=	number of mole of Mn dopant

α	=	the ratio of τ_R to τ_{NR}
β	=	the full width half maximum intensity (FWHM)
γ	=	the water/oil interfacial tension (IFT)
η	=	quantum yield
η_V	=	viscosity
θ	=	Bragg angle of diffraction peak
λ	=	CuKα radiation wavelength (λ = 1.5406 Å)
λ_e	=	electron wavelength
υ	=	transition diffusion coefficient
ν_{th}	=	the thermal velocity of an electron
σ	=	the centre size of an electron
$1/\tau_R$	=	band-to-band recombination rate
$1/\tau_{NR}$	=	nonradiative recombination rate

APPENDIX B

CALCULATED CRYSTALLINE PLANES BY SELECTED-AREA ELECTRON DIFFRACTION (SAED) IMAGE

Crystalline planes are calculated by Camera equation (equation B1). Where R_C, d_{SAED}, λ_e and L_C are radius of crystalline plane, d-spacing calculated by SAED, electron wavelength and camera length, respectively [92,93].

$$R_C d_{SAED} = \lambda_e L_C \quad \text{(B1)}$$

For the parameter of camera length is calculated by equation B2 where l and n are bar length and number on bar in SAED image as illustrated in Figure B1, respectively [93].

$$L_C = \frac{l}{n\lambda_e} \quad \text{(B2)}$$

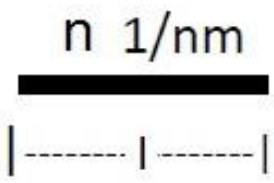

Figure B1 Bar in SAED image

Parameter of l and n were shown in Figure B1. Then, the calculating d_{SAED} value from equation B1 added in equation B3 and calculated $(h^2+k^2+l^2)$ value. Parameter of a and $(h^2+k^2+l^2)$ in equation B3 are lattice parameter (as shown in JCPDs) and miller indices, respectively. However, equation B3 only uses in cubic crystalline structure case. Finally, $(h^2+k^2+l^2)$ compared crystalline plane {h, k, l} in Table B1.

$$\frac{1}{d_{SAED}^2} = \frac{(h^2+k^2+l^2)}{a^2} \quad \text{(B3)}$$

Table B1 Possible $(h^2 + k^2 + l^2)$ values at different crystalline planes [92]

$(h^2 + k^2 + l^2)$	{h, k, l}
1	100
2	110
3	111
4	200
5	210
6	211
7	-
8	220
9	221 or 300
10	310
11	311
12	222
13	320
14	321

Example: Mn-doped ZnS nanoparticle were synthesized by micro-emulsion method at W=3 and Mn concentration = 1% by weight. SAED image of Mn-doped ZnS nanoparticles were shown in Figure B2.

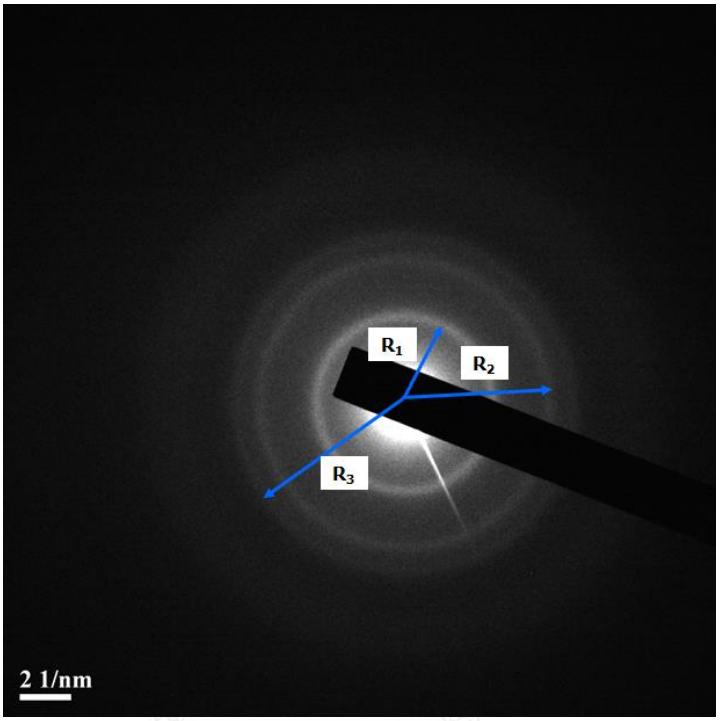

Figure B2 SAED image of Mn-doped ZnS nanoparticles synthesized by micro-emulsion at W=3 and C_{Mn} = 1 wt. %.

- Calculated L_C by equation B2 where l = 1.0 cm, n = 2 /nm and λ_e = 0.003 nm.

$$L_C = \frac{1.0\ \text{cm}}{\frac{2}{\text{nm}} \times 0.003\text{nm}} = 167\ \text{cm}$$

- Calculated d_{SAED} by equation B1 where R1 = 1.6 cm, R2 = 2.6 cm and R3 = 3.1 cm, respectively.

$$d_{SAED,1} = \frac{\lambda_e L_C}{R_1} = \frac{0.003\ \text{nm} \times 167\ \text{cm}}{1.6\ \text{cm}} = 0.31\ \text{nm}$$

$$d_{SAED,2} = \frac{\lambda_e L_C}{R_2} = \frac{0.003\ \text{nm} \times 167\ \text{cm}}{2.6\ \text{cm}} = 0.19\ \text{nm}$$

$$d_{SAED,3} = \frac{\lambda_e L_C}{R_3} = \frac{0.003\ \text{nm} \times 167\ \text{cm}}{3.1\ \text{cm}} = 0.16\ \text{nm}$$

- Calculated ($h^2 + k^2 + l^2$) by equation B3 where a = 0.54110 nm (JCPDs 01-089-4958)

$$(h^2 + k^2 + l^2) = \frac{a^2}{d^2_{SAED,1}} = \frac{0.54110^2\ \text{nm}^2}{0.31^2\ \text{nm}^2} = 2.8 \approx 3$$

$$(h^2 + k^2 + l^2) = \frac{a^2}{d^2_{SAED,2}} = \frac{0.54110^2\ \text{nm}^2}{0.19^2\ \text{nm}^2} = 7.9 \approx 8$$

$$(h^2 + k^2 + l^2) = \frac{a^2}{d^2_{SAED,3}} = \frac{0.54110^2\ \text{nm}^2}{0.16^2\ \text{nm}^2} = 11.3 \approx 11$$

- Comparison between ($h^2 + k^2 + l^2$) value and crystalline plane in Table C1.

Therefore, crystalline planes of Mn-doped ZnS nanoparticles at W=3 consist of (1 1 1), (2 2 0) and (3 1 1).

APPENDIX C

CALCULATED K-SPACE AND RADIAL DISTANCE BY ENERGY DATA OF EXAFS

Definition of EXAFS structure is shown in equation C1. Where μ (E) and μ_0 (E) are sample absorption and atomic background absorption, respectively [103,104]. EXAFS spectra of this definition were plotted in Figure C1. Figure C1 are the normalized EXAFS spectra of Mn-doped ZnS nanoparticles at Mn K-edge.

$$\chi(E) = \frac{\mu(E)-\mu_0(E)}{\mu_0(E)} \quad \text{(C1)}$$

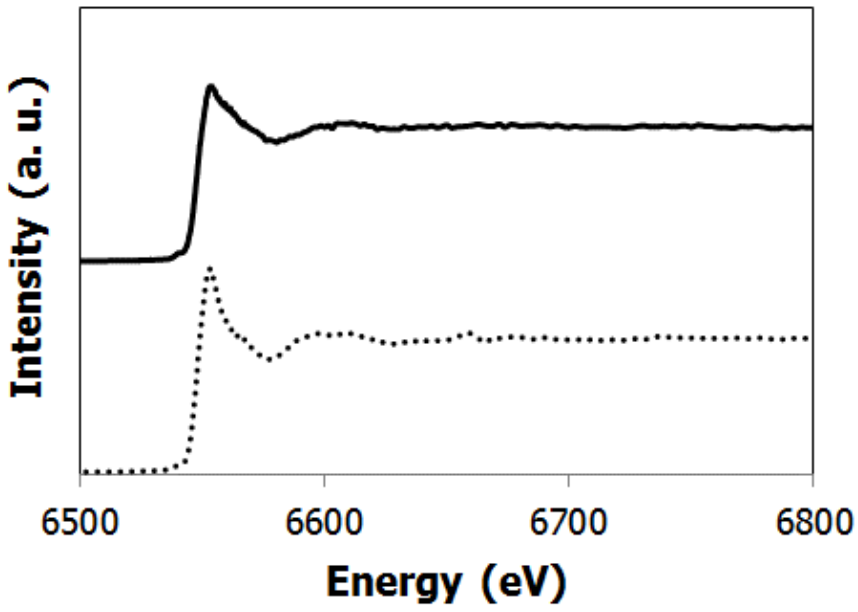

Figure C1 Normalized EXAFS spectra of Mn-doped ZnS nanoparticle at Mn K-edge: 6% Mn-doped ZnS nanoparticles (solid line) and 10% Mn-doped ZnS nanoparticles (dot line)

EXAFS structure can be writen in sine function of parameter k and R as shown in equation C2. Where k and R are wavenumber and distance between absorbed atom and neighbor atom or radial distance, respectively [103,104]. Wavenumber can be calculated by X-ray energy in equation C1. Figure C2 shows sine function of k-space of Mn-doped ZnS nanoparticles at Mn K-edge.

$$\chi(k) = \left|\sum A_j k\right| \sin\left(2kR_j + \delta_j(k)\right) \quad \text{(C2)}$$

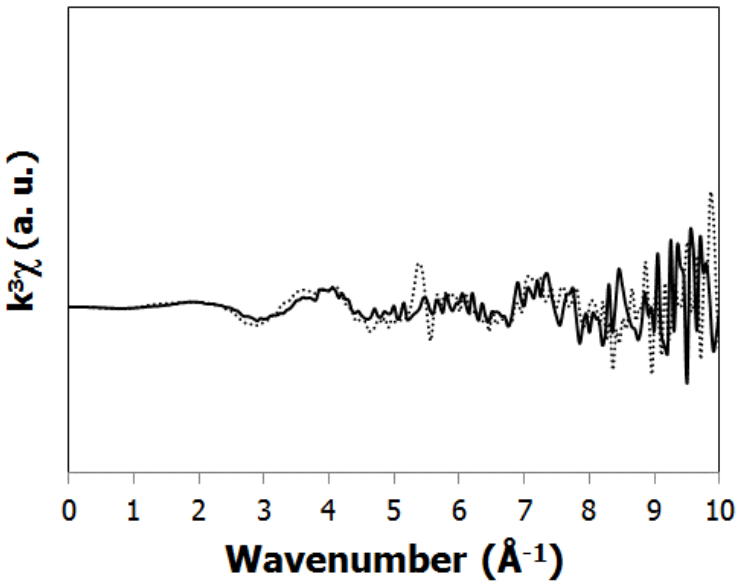

Figure C2 K-space of Mn-doped ZnS nanoparticles at Mn K-edge: 6% Mn-doped ZnS nanoparticles (solid line) and 10% Mn-doped ZnS nanoparticles (dot line)

In equation C2, χ (k) was written in summation of scattering signal. It can consider scattering signal in each level of atom type. Each term in equation C2 with the same type of atom consist of amplitude and scattering phase. Amplitude of EXAFS is defined by equation C3.

$$A_j(k) = S_0^2 \frac{N_j S_j(k,R_j) F_j(k,R_j)}{kR_j^2} \exp\left[\frac{-2R_j}{\lambda(k,R_j)}\right] \exp(-2\sigma_j^2 k^2) \quad \text{(C3)}$$

Where S_0, N_j, S_j, F_j, R_j, λ_j and σ_j are scale factor, number of j atom, total loss factor, effective EXAFS scattering amplitude, distance between absorbed atom and neighbor atom or radial distance, photoelectron mean free path and Debye-Waller factor [103,104].

Analysis of EXAFS structure used Fourier transformation for transformed function of k parameter to R parameter. After transformation, EXAFS structure become function of R parameter at defined and represented in equation C4 [103,104] and Figure C3, respectively.

$$\chi(R) = \frac{1}{\sqrt{\pi}} \int \chi(k) k^n e^{2ikR} dk \quad \text{(C4)}$$

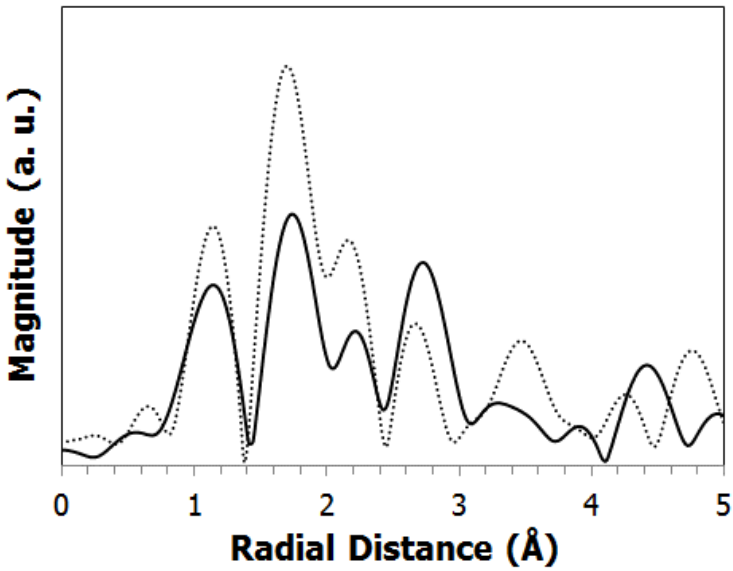

Figure C3 Fourier transformed spectra of Mn K-edge EXAFS function for Mn-doped ZnS nanoparticles: 6% Mn-doped ZnS (Solid line) and 10% Mn-doped ZnS (dot line)

APPENDIX D

CALCULATE AMOUNT OF MN-DOPED ZNS NANOPARTICLES PRODUCT

BY THEORY

Chemical reaction of Mn-doped ZnS is the precipitation reaction. It is an irreversible reaction. When assuming Mn concentration is very low, the amount of Mn-doped ZnS nanoparticles product can be used the precipitation reaction of ZnS for easier calculation. The precipitation reaction of ZnS is shown in equation D1.

$$ZnSO_{4\,(aq)} + Na_2S_{(aq)} \rightarrow ZnS_{(s)} + Na_2SO_{4\,(aq)} \qquad \text{(D1)}$$

Example: Synthesis of Mn-doped ZnS nanoparticles at W=1, [$ZnSO_4$] = 0.099 M, [$MnSO_4$] = 0.001 M and [Na_2S] = 0.10 M. Molecular weight (MW) of ZnS is 97.469 g/mole. Volume of water phase in micro-emulsion system (V) at W=1 is 0.90 ml.

From equation D1, mole of Na_2S is depleted consumption with assuming complete reaction.

$$ZnSO_{4\,(aq)} + Na_2S_{(aq)} \rightarrow ZnS_{(s)} + Na_2SO_{4\,(aq)}$$

$$\text{Mole of } Na_2S \text{ consumption} = \text{Mole of ZnS product}$$

$$\frac{MV}{1000} = \frac{\text{grams of ZnS}}{MW}$$

$$0.1\ \frac{\text{mole}}{\text{L}} \times 0.9\ \text{ml} \times \frac{1\ \text{L}}{1000\ \text{ml}} = \frac{\text{grams of ZnS}}{97.469\ \frac{\text{g}}{\text{mole}}}$$

$$\text{grams of ZnS} = 0.0088\ \text{grams}$$

APPENDIX E

MORPHOLOGY AND PARTICLE SIZE OF MN-DOPED ZNS NANOPARTICLES CHARACTERIZED BY TEM

The averaged primary particle sizes were also characterized by TEM as shown in Figure E1. For TEM images, the spherical shape of the primary particle of Mn-doped ZnS nanoparticles are agglomeration. The averaged primary particle size and standard deviation are 4±1, 6±1, 8±1, 10±2, 12±1and 16±3 at W=1, 3, 5, 7, 11 and 15, respectively. Figure E2 shows dependence of the averaged primary particle size of Mn-doped ZnS nanoparticles with the molar ratio of water to surfactant. At increased W values, the averaged primary particle size of Mn-doped ZnS becomes larger. These results are in good agreement with the many previous study [36,66,75-77,80-87]. The morphology of Mn-doped ZnS nanoparticles and trend of the averaged primary particle size at various W values were consistent with FE-SEM result.

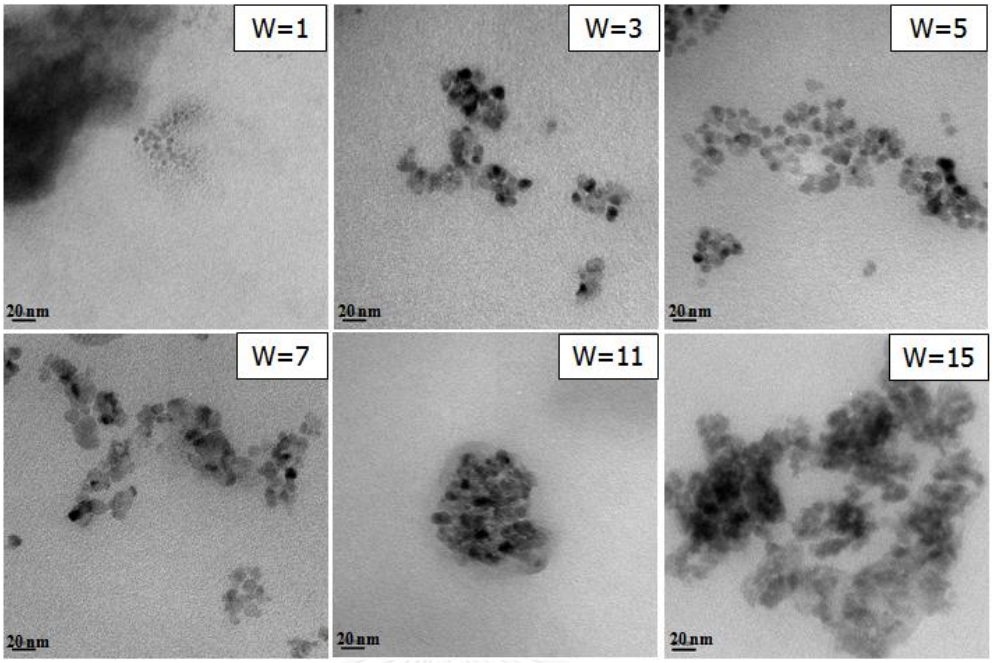

Figure E1 TEM images of Mn-doped ZnS nanoparticles at various W values

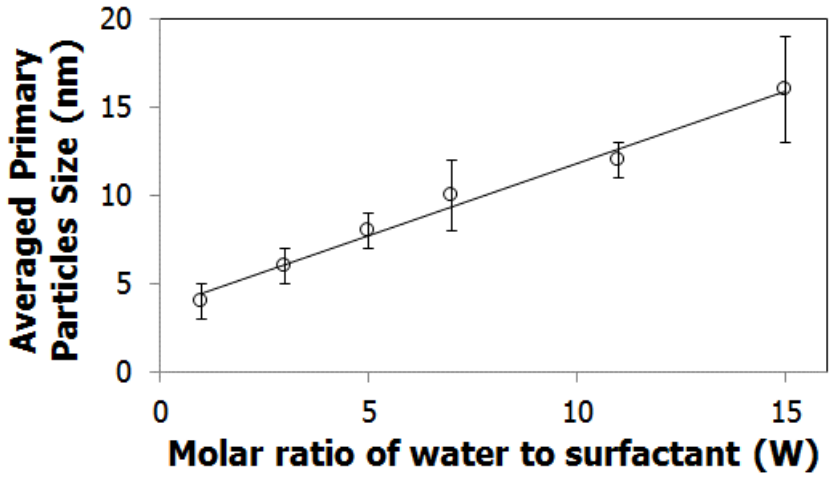

Figure E2 Dependence of the molar ratio of water to surfactant on the averaged primary particles size analyzed by TEM images

APPENDIX F

SYNTHESIZED MN-DOPED ZNS NANOPARTICLES BY PREFABRICATED MICRO-EMULSION

Mn-doped ZnS nanoparticles synthesized by prefabricated micro-emulsion for increasing amount of Mn-doped ZnS nanoparticles product. Concentration of $ZnSO_4$, $MnSO_4$ and Na_2S were 0.099 M, 0.001 M and 0.10 M, respectively. This experiment is conducted under room temperature of 30°C. Micro-emulsion system used W=7 while volume of water phase is equal volume of solution. The morphology, the primary particle size and crystalline structure were analyzed by FE-SEM, XRD, SAED and HRTEM, respectively. Higher amount of Mn-doped ZnS nanoparticles product can be promoted Mn-doped ZnS nanoparticles and its application.

The morphology, the primary particle size and particle size distribution of Mn-doped ZnS nanoparticles synthesized by prefabricated micro-emulsion were shown in Figure F1. Mn-doped ZnS nanoparticles are agglomeration of spherical shape. The averaged primary particle size is 20±7 nm.

XRD pattern of Mn-doped ZnS nanoparticles synthesized by prefabricated micro-emulsion was illustrated in Figure F2. The three peaks of this nanoparticle appeared at 29.08° (1 1 1), 48.08° (2 2 0) and 56.52° (3 1 1) relative to the standard card (JCPDs 01-089-4958) which is also consistent with SAED (Figure F3). This XRD pattern confirmed these samples consist of Mn and ZnS crystals which co-exist as zinc blend crystalline structure.

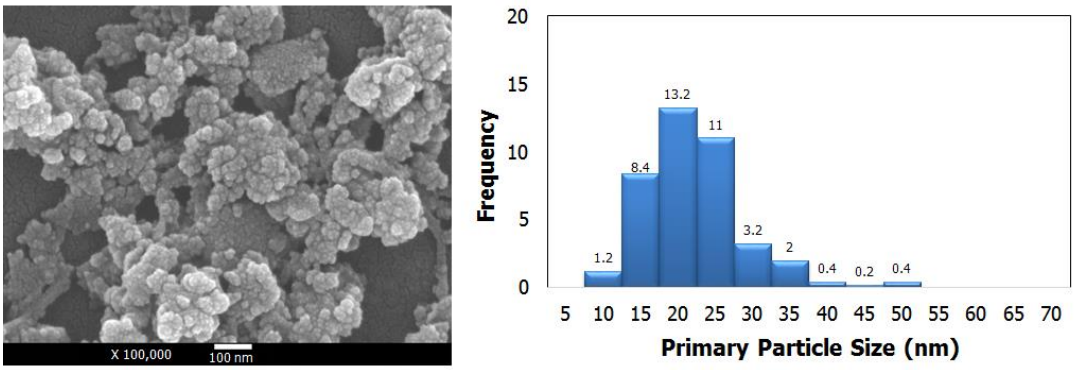

Figure F1 FE-SEM image and particle size distribution of Mn-doped ZnS nanoparticles synthesized by prefabricated micro-emulsion

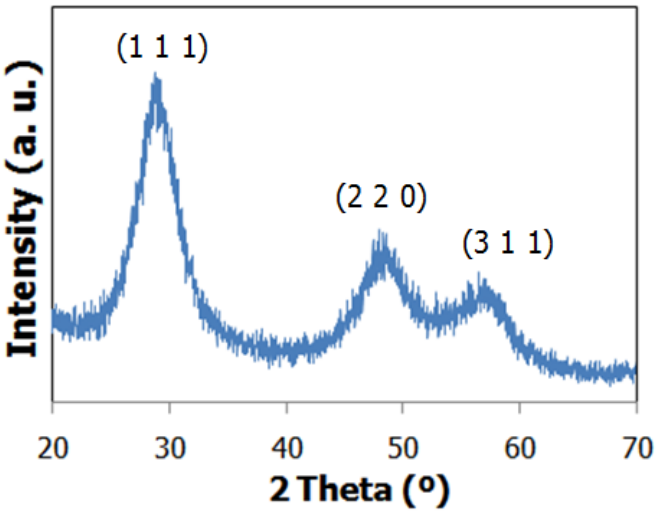

Figure F2 XRD pattern of Mn-doped ZnS nanoparticles synthesized by prefabricated micro-emulsion

The microcrystalline structure of Mn-doped ZnS nanoparticles synthesized by prefabricated micro-emulsion was zinc blend crystalline structure that were confirmed by SAED (Figure F3). This result is in a good agreement with XRD pattern. Mn-doped ZnS nanoparticles was polycrystalline that was confirmed by SAED and HRTEM images

as shown in Figure F3. In addition, SAED image appears crystalline planes of (1 1 1), (2 2 0) and (3 1 1). Three crystalline planes are in good agreement with zinc blend crystalline structure that was consistent with XRD pattern in Figure F2.

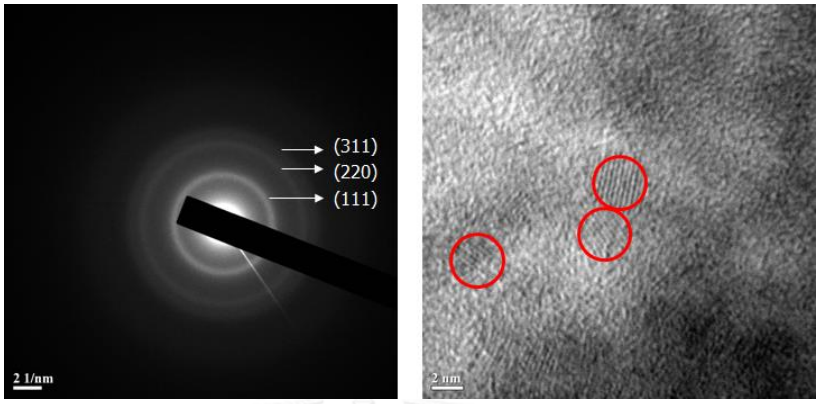

Figure F3 SAED and HRTEM image of Mn-doped ZnS nanoparticles synthesized by prefabricated micro-emulsion

Comparison between the amount of product synthesized by micro-emulsion at W=1 and the amount of product synthesized prefabricated micro-emulsion at W=7 was shown in Figure F4. Amount of product of Mn-doped ZnS nanoparticles synthesized by prefabricated micro-emulsion is higher from 8 to 55 milligrams. Unfortunately, these results cannot explanation now but they are interesting in the further investigation.

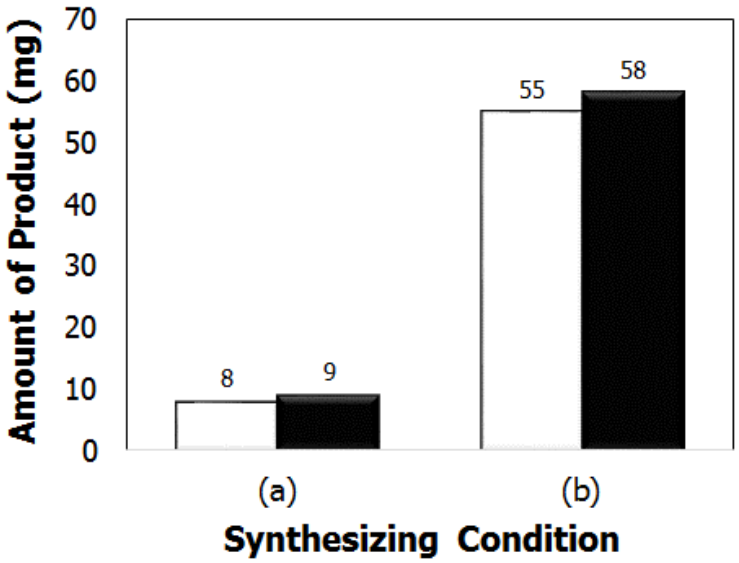

Figure F4 Comparable amount of product synthesized by: (a) micro-emulsion at W=1 and (b) prefabricated micro-emulsion at W=7 as experiment (white) and theory (black)

VITA

Mr. Nattanai Rungrotmongkon was born on 14 November 1988. In 2006, he graduated from high school at Donmuang Chaturachinda School, Bangkok. In 2010, he received bachelor degree at Chemical Engineering, Faculty of Engineering, Thammasart University. And then he received master degree at Chemical Engineering, Faculty of Engineering, Chulalongkorn University in 2014.